Nuclear dynamics of the Set1C subunit Spp1 prepares meiotic recombination sites for break formation

Zsolt Karanyi, Laszlo Halasz, Laurent Acquaviva, David Jonas, Szabolcs Hetey, Beata Boros-Olah, Feng Peng, Doris Chen, Franz Klein, Vincent Geli, et al.

HAL Id: hal-02143597
https://amu.hal.science/hal-02143597

Submitted on 3 Jun 2019

ARTICLE

Nuclear dynamics of the Set1C subunit Spp1 prepares meiotic recombination sites for break formation

Zsolt Karányi[1,2], László Halász[1] , Laurent Acquaviva[3] , Dávid Jónás[1], Szabolcs Hetey[1], Beáta Boros-Oláh[1], Feng Peng[4], Doris Chen[4] , Franz Klein[4], Vincent Géli[3]* , and Lóránt Székvölgyi[1]*

Spp1 is the H3K4me3 reader subunit of the Set1 complex (COMPASS/Set1C) that contributes to the mechanism by which meiotic DNA break sites are mechanistically selected. We previously proposed a model in which Spp1 interacts with H3K4me3 and the chromosome axis protein Mer2 that leads to DSB formation. Here we show that spatial interactions of Spp1 and Mer2 occur independently of Set1C. Spp1 exhibits dynamic chromatin binding features during meiosis, with many de novo appearing and disappearing binding sites. Spp1 chromatin binding dynamics depends on its PHD finger and Mer2-interacting domain and on modifiable histone residues (H3R2/K4). Remarkably, association of Spp1 with Mer2 axial sites reduces the effective turnover rate and diffusion coefficient of Spp1 upon chromatin binding, compared with other Set1C subunits. Our results indicate that "chromosomal turnover rate" is a major molecular determinant of Spp1 function in the framework of meiotic chromatin structure that prepares recombination initiation sites for break formation.

Introduction

Regulation of chromatin structure through covalent histone modifications is a central mechanism for modulating DNA-directed biological processes, including gene transcription, mRNA processing, and DNA replication, recombination, and repair. Histone modifications act by directly altering the chromatin structure or by creating docking sites that facilitate the binding of chromatin readers (Rothbart and Strahl, 2014). These readers in turn recruit remodeling enzymes or additional chromatin modifiers (Tessarz and Kouzarides, 2014). In the past years, methylation of lysine 4 on histone H3 (H3K4) has received considerable attention and was linked to several aspects of transcriptional regulation (Ruthenburg et al., 2007) and class-switch recombination (Daniel et al., 2010), S-phase DNA damage checkpoint (Liu et al., 2010), and meiotic recombination (Borde and de Massy, 2013). The family of H3K4 methylases is highly conserved from yeast to human (Shilatifard, 2012). They share a canonical organization in which the catalytic subunit acts as a docking platform for multiple subunits that regulates the activity of the enzyme (Ernst and Vakoc, 2012). The budding yeast Set1 complex has proved to be an excellent model to study the *SET1/MLL* family complexes. In *Saccharomyces cerevisiae*, all H3K4 methylation is performed by a complex called Complex of Proteins Associated with Set1 (COMPASS; Miller et al., 2001) or Set1C (Roguev et al.,

2001) composed of Set1, the catalytic subunit, acting as a scaffold for seven other components (Swd1 [RbBP5], Swd2 [Wdr82], Swd3 [Wdr5], Bre2 [Ashl2], Sdc1 [Dpy30], Spp1 [Cfp1], and Shg1 [Bod1]; Miller et al., 2001; Nagy et al., 2002). In the past years, several studies contributed to define how each subunit of Set1C was bound to the docking platform established by the catalytic Set1 subunit. Swd1, Swd3, Bre2, and Sdc1 were shown to interact with the isolated SET domain to form the SET-c (Dehé et al., 2006; Trésaugues et al., 2006; Kim et al., 2013). On the other hand, Spp1, Swd2, and Shg1 directly interact with the n-SET domain, the N-terminal domain, and the second RNA-recognition motif (RRM) motif of Set1, respectively (Dehé et al., 2006; Halbach et al., 2009; Kim et al., 2013). Loss of individual Set1C subunits differentially affects Set1 stability, complex integrity, global H3K4 methylation patterns, and H3K4 methylation along active genes (Soares et al., 2014).

The recruitment of Set1C to chromatin is not fully understood. Set1C has been shown to be targeted to the 5′ regions of transcription units via the Paf1C elongation factor and the CTD of Pol II (Krogan et al., 2003; Ng et al., 2003). These interactions are thought to contribute to the prevalence of H3K4me3 at chromatin domains at the 5′-end of active genes. However, directly interacting protein(s) that would recruit Set1C to actively tran-

scribed genes have not yet been identified. Recently, Set1C was shown to bind mRNAs in vitro and in vivo (Trésaugues et al., 2006; Battaglia et al., 2017; Luciano et al., 2017; Sayou et al., 2017). Unexpectedly, multiple protein surfaces in Set1C, as well as the dRRM, N-SET domain, and Spp1, were shown to be important to bind RNA in vitro. RNA binding of Set1 was found to be important for the proper topology of Set1C distribution along transcription units (Luciano et al., 2017; Sayou et al., 2017).

Meiosis is a differentiation process involving two successive cell divisions required for the formation of haploid nuclei and gametes from germ cells (Székvölgyi and Nicolas, 2010; Székvölgyi et al., 2015). During the first meiotic division, meiotic recombination is initiated by the formation of DNA double-strand breaks (DSBs) catalyzed by the meiosis-specific type II topoisomerase-like DNA transesterase Spo11 (Keeney et al., 1997). In *S. cerevisiae*, DSBs localize to specific regions called hot spots that mainly overlap with nucleosome depleted intergenic regions, near promoters (Pan et al., 2011). DSB formation also requires several Spo11-associated proteins that form sub-complexes (Lam and Keeney, 2015). The Mer2/Mei4/Rec114 (RMM) sub-complex has been proposed to link DSB sites located within chromatin loops to chromosome axial structures to undergo Spo11-mediated cleavage (Panizza et al., 2011). It was initially observed that Set1 inactivation severely reduced the level and distribution of meiotic DNA breaks (Sollier et al., 2004). Moreover, nucleosomes flanking DSB sites were shown to be enriched in histone H3K4 trimethylation that was independent of the mRNA expression level of nearby genes (Borde et al., 2009). Consistent with these observations, inactivation of *RAD6* (Yamashita et al., 2004) or the PAF1 complex (Gothwal et al., 2016) that both reduce H3K4 methylation significantly also reduced meiotic DSB frequencies; however, this by itself did not prove that H3K4me directly promoted DSB formation. The link between H3K4me3 and meiotic DNA breaks is conserved in many organisms including mammals, where the H3K4me3 mark is deposited by a sequence-specific histone methylase, Prdm9, which directs DSBs to certain DNA motifs recognized by its zinc finger domain (Baudat et al., 2010; Parvanov et al., 2010).

The mechanism by which H3K4 methylation is linked to DSB formation was further highlighted by the discovery that Spp1 (the PHD-finger subunit of Set1C) can physically interact with both H3K4me2/3 and Mer2, located at the meiotic chromosomal axis (Acquaviva et al., 2013b; Sommermeyer et al., 2013). It was proposed that the interaction between Spp1 and Mer2 anchors meiotic DSB hot spots to the chromosome axis for downstream events that will ultimately lead to Spo11-dependent DSB formation at axis-proximal regions (Acquaviva et al., 2013a). This model proposed an explanation of how chromosome architecture and DSB regulation are interrelated at the molecular level and revealed the key role of Spp1 in recruiting meiotic DSB sites to the chromosome axis.

The above data demonstrate that Spp1 not only regulates the catalytic activity of Set1C, but also interacts with the deposited H3K4me3 mark and mediates its downstream effects. Remarkably, dissociation of Spp1 from Set1C repurposed its biological function to promote epigenetic transcriptional memory at the *INO1* gene (D'Urso et al., 2016). These results refer to the highly

dynamic behavior of Spp1; however, the nuclear dynamics of Set1C subunits have not been directly and systematically studied to date. The temporal and spatial sequence of events controlling the chromatin binding of Set1C and the exact molecular mechanism of Spp1 chromosomal redistribution during meiosis have also remained important unanswered questions.

Here, we used dynamic chromatin mapping and quantitative imaging to unravel the chromatin binding characteristics and turnover rate of Set1C and Spp1 in live meiotic nuclei. We present a detailed spatio-temporal picture showing how Spp1 becomes redistributed from actively transcribed genes to chromosome axial sites, independently of Set1C.

Results

Spp1 and Mer2 partially colocalize in meiotic chromosome spreads

Since Spp1 was shown to physically interact with Mer2 and to bind to Mer2 chromosomal sites at the time of meiotic DSB formation (Acquaviva et al., 2013b; Sommermeyer et al., 2013; Adam et al., 2018), we tagged Spp1/Mer2 (and Bre2/Mer2) to perform double-immunofluorescence labeling on meiotic chromosome spreads to ascertain whether Spp1/Mer2 would colocalize in one and the same nucleus by the time of DSB formation. Cells coexpressing Mer2 internally tagged with 3xHA, Mer2-HA.int, and Spp1-myc (or Bre2-myc) as their only source for these proteins were synchronized, and samples were collected at different time points during the meiotic time course. As exemplified in Fig. 1 A, Spp1 and Mer2 foci colocalized 4 h after transfer to sporulation medium (SPM), whereas Bre2 and Mer2 foci (Fig. 1 B) did not. Quantification of Spp1 foci overlapping with Mer2 showed colocalization for all time points analyzed, reaching a plateau at 3–6 h after transfer to SPM, with ~50% of Spp1 foci overlapping with Mer2 foci (Fig. 1 C). To assign statistical significance for colocalization frequencies, we simulated random colocalization using FociSim (Kurzbauer et al., 2012). For each nucleus, Monte Carlo simulations with 200,000 random seeds were performed, with nuclear area, foci numbers, and foci areas from the experimental data, yielding a distribution of random overlaps (dashed lines in Fig. 1, C–F). Colocalization was significant for each of the analyzed wild-type nuclei (n = 25) based on random simulations at all time points (P < 0.02; Table S1). Moreover, colocalizations per time point were also significantly higher than random overlaps (Welch's t test, P < 0.001 for 3, 4, and 5 h in SPM; Fig. 1 C and Table S1). In particular, Mer2 foci numbers showed a dynamic behavior, with fewer foci at time points 2 and 6 h in SPM (Fig. 1 H), contributing to the slightly lower colocalization at these time points. We next analyzed the colocalization of Mer2 with two Spp1 mutants whose function in bridging H3K4 and Mer2 is impaired: Spp1CxxCΔ (Fig. 1 D) lacks the CxxC zinc finger motif involved in Mer2-Spp1 interaction at chromosomal axis sites, while Spp1PHDΔ (Fig. 1 E) contains a truncation of the PHD finger domain that affects the binding of Spp1 to H3K4 trimethylated nucleosomes (Acquaviva et al., 2013b). Both mutants showed a decreased Spp1 focus number, but did not change Mer2 focus counts (Fig. 1, G and H). Although the number of potential Mer2 partner foci was unchanged, the proportion of colocalizing

Spp1 foci decreased significantly compared with wild-type cells (Welch's *t* test, P ≤ 0.02 for 3, 4, 5, and 6 h in SPM; Fig. 1 D and E and Table S1). Colocalization reached a plateau only in 30% of both mutants, which was still higher than randomized colocalization (Welch's *t* test, P < 0.01 for 2, 3, 5 h for Spp1CxxCΔ; and P < 0.05 for 2, 3, 5 h in SPM for Spp1PHDΔ; Table S1). Colocalization of Mer2 with the Set1 subunit Bre2 that stably interacts with Set1C (see below) was lower or equal than assumed from a random distribution (Welch's *t* test, P > 0.1; not significant for all time points; Table S1); however, it was significantly lower than that of Spp1-Mer2 (Welch's *t* test, P < 0.01; Fig. 1 F and Table S1). Together, these data highlight spatial associations between Mer2 and Spp1 that are snot seen between Mer2 and the Set1C/Bre2 holocomplex. Wild-type level of association requires Spp1's Mer2 and H3K4me3 interaction motifs, suggesting that these domains critically enhance the lifespan of the observed interactions.

Spp1 exhibits static and dynamic chromosome binding kinetics during meiosis

To assess the chromatin dynamics of Spp1 during the progression of meiotic prophase, we mapped the chromosomal locations of epitope-tagged Spp1 and Bre2 by chromatin immunoprecipitation (ChIP) sequencing in synchronously sporulating yeast cultures (Fig. S1). The distribution of Bre2 was used as a proxy to mark the chromosomal position of Set1C. Peak sets identified at individual meiotic time points (pre-SPM [SPS]; 0, 2, 4, and 6 h in SPM) were concatenated and sorted by chromosomal position and then merged (all peaks and ChIP-seq profiles established in this study can be accessed via JBrowse, see Materials and methods for details). Venn diagram analysis of chromatin binding sites shows that ~46% of the Spp1 peaks coincide with Bre2 (Fig. 2 A), which may represent a group of Spp1 molecules associated with Set1C during meiosis.

Overall, Spp1 and Bre2 (common) peaks and Bre2-only peaks show strong enrichment on ribosomal protein genes (RPGs), snoRNA/ncRNA genes and transcription start sites (TSSs), but they are absent from Mer2/Red1 axial sites (Fig. 2 B), as defined by genome-wide ChIP analysis (Panizza et al., 2011; Sun et al., 2015). In contrast, Spp1-only peaks are significantly overrepresented at Mer2/Red1 sites. Strikingly, Bre2-only peaks are highly enriched at RPG and tRNA genes compared with common peaks of Spp1 and Bre2, indicating the presence of Spp1-free Set1C on these genes during meiosis.

Importantly, Spp1 showed a progressive loading onto Mer2 binding sites during meiotic prophase, while Bre2 remained depleted throughout the sporulation process (Fig. 2 C). Although Spp1 binding sites appear to be more dynamic than common (Spp1 and Bre2) sites (representative JBrowse example for dynamic Spp1 peaks is shown in Fig. 2 D), the latter peaks show much higher ChIP signal compared with Spp1-only or Bre2-only sites (ANOVA with Tukey HSD, P < 0.0001; Fig. 2 E). We explain these differences with the differential turnover rate characteristics of the sites (see below).

To gain more mechanistic insights into the dynamics of Spp1, we performed k-means clustering analysis on the time-resolved Spp1 ChIP signals, classifying the identified binding sites based on their similarity (see Materials and methods). Two kinetic frac-

tions were readily revealed based on the relative change of Spp1 peak signals over time (Fig. 2 F): dynamic sites, which gradually appeared (red) or disappeared (blue) as meiosis progressed, and static sites (green) showing permanent association with Spp1. These separate classes were reproduced by a clustering-independent approach that relied on the absolute change of Spp1 signal intensities in terms of time (Fig. 2 G; see legend for explanation).

Functional annotation revealed that (1) appearing Spp1 peaks are strongly enriched at chromosome axial sites (Red1 and Mer2), (2) disappearing Spp1 sites are enriched at RPG and snoRNA genes, and (3) constant Spp1 peaks show strong association with ncRNAs (Fig. 2 H). We conclude that the dynamic properties of Spp1 correlate with its noncanonical (Set1C independent) functions and the remodeling of Set1C at RPG and snoRNA genes during the meiotic process.

Functional analysis of Spp1 chromatin binding in meiosis

To further shed light on the molecular determinants of Spp1 chromatin binding, we also examined the binding sites of Spp1PHDΔ and Spp1CxxCΔ mutants and that of H3R2A and H3K4R mutants. Mutation of lysine 4 prevents H3K4 methylation, while substitution of arginine 2 by alanine inhibits the deposition of H3K4me3 (Kirmizis et al., 2007; Yuan et al., 2012). Both modifications are expected to phenocopy the meiotic phenotype of the Spp1PHDΔ mutation (Fig. 3 A). We performed time-resolved meiotic ChIP-seq and mapped the binding of Spp1PHDΔ, Spp1CxxCΔ, and Spp1 in H3R2A/H3K4R mutants (the data can be accessed through JBrowse; see Materials and methods). As shown in Venn diagrams (Fig. 3 B), all four mutations eliminate ~50% of Spp1 binding sites during the meiotic time-course identified in the wild-type strain. Interestingly, some new Spp1 sites (~10%) are also generated in each mutant (Fig. 3 B).

We next performed multidimensional scaling (MDS) analysis on the identified binding sites to highlight temporal and cell type–specific differences in Spp1 chromosomal localization (Fig. 3 C). For all cell types and meiotic time points, exact chromosomal position and enrichment of all the identified Spp1 ChIP peaks were assigned to N-dimensional coordinates, defining Spp1 "states" by cell type and meiotic stage. All Spp1 states were then projected to a 2D plane (highlighted as dots in the MDS maps, Fig. 3 C) such that the closer is the difference between any two datapoints the more similar the Spp1 states are. As shown in the upper panel of Fig. 3 C, wild-type cells and Spp1 PHD- and CxxC-domain mutants behave very differently at the beginning of sporulation. Then, in the first 2 h, there will be a large, rapid, and identical change in both wild-type and mutant cells. By the end of the process, each cell type converges to a similar Spp1 state, which is shown by the small distance of dots at the 6-h time point. In the histone mutant backgrounds (lower panel in Fig. 3 C), Spp1 binding sites are more similar to the wild type at the beginning of sporulation (0 h in SPM). Subsequently, fast and dynamic changes occur in the first few hours such that both mutants quickly move away from the wild type. By the end of the process all three cell types are characterized by a different Spp1 state.

We next analyzed the overlap of Spp1 binding sites with annotated functional genomic elements in each mutant (Spp1PHDΔ, Spp1CxxCΔ, H3R2A, and H3K4R). As shown in Fig. 3 D, the result-
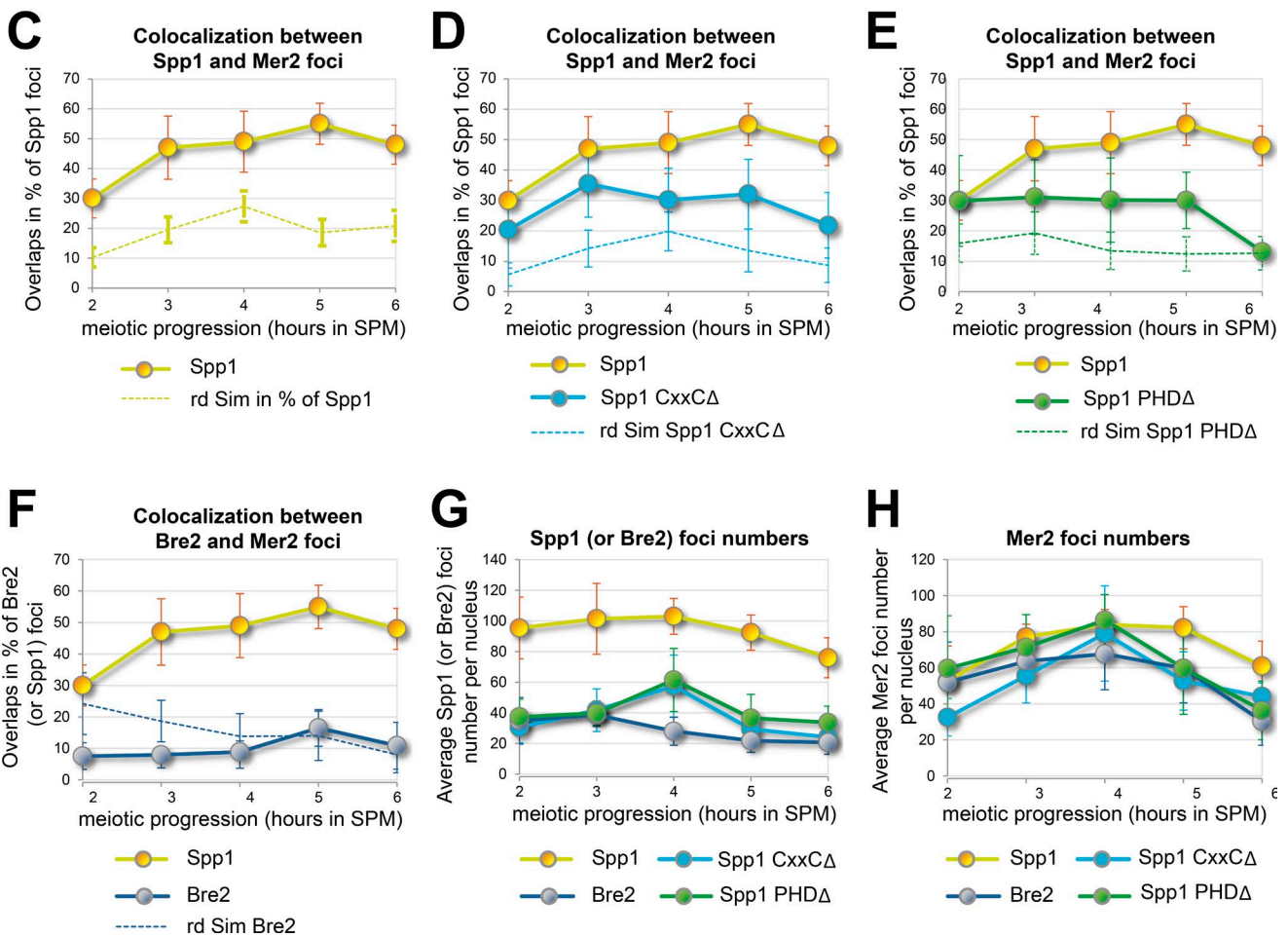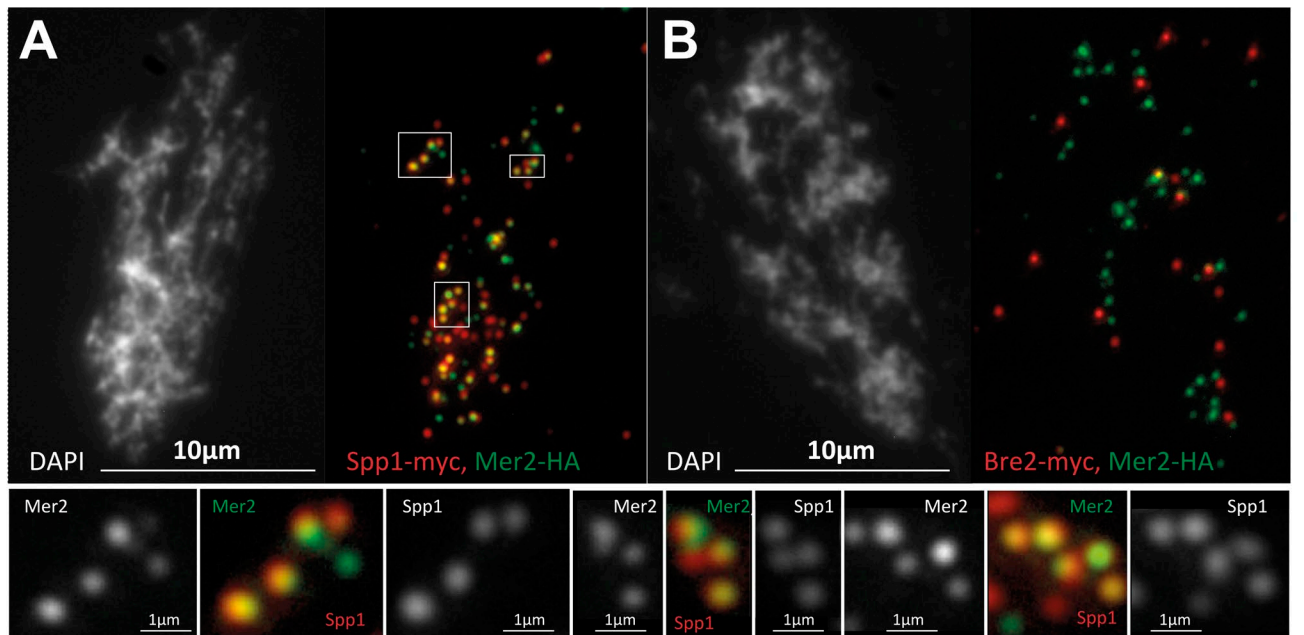
Figure 1. **Localization of Spp1-myc, Bre2-myc, and Mer2-HA in meiotic chromosome spreads and quantification of overlaps. (A)** Representative chromatin spread showing Spp1-myc foci (red) and Mer2-HA.int foci (green). Insets are also displayed at higher magnification in lower panels. **(B)** The same as A, but Bre2-myc (red) and Mer2-HA.int (green) foci are shown. Cells were taken from a meiotic time course at 4 h after transfer to SPM. DNA was stained by DAPI (white). **(C–E)** The graphs show the percentage of Spp1-myc foci overlapping with Mer2-HA.int in wild-type cells (yellow; C), and in Spp1CxxCΔ-myc (light blue; D), and Spp1PHDΔ-myc mutants (green; E). **(G)** Expressing overlap in percentage of Spp1 foci demonstrates changes in the overlap ratio between Spp1 and Mer2 independent of the reduction in Spp1 foci numbers seen in the mutants. **(F)** Percentage of Bre2-myc foci overlapping with Mer2-HA.int (gray). **(C–F)**

ing peaks are differentially enriched over several genomic elements and show variable overlap with each other (from 7 to 58%; Fig. S2 A). Importantly, all mutations reduce the binding of Spp1 to axis sites (Fig. 3 D) and abrogate the association of dynamic clusters of Spp1 peaks with Mer2 sites (Fig. 3 E). The PHDΔ mutant shows a very high enrichment of Spp1 at RPG genes, which highlights the role of the PHD domain in the removal of Spp1 from RPG genes (Fig. 3 D). Similarly, H3R2A and H3K4R mutants exhibit specific Spp1 enrichment at snoRNA genes, indicating that H3R2 and H3K4 methylation promotes the disappearance of Spp1 from snoRNAs.

The heat maps shown in Fig. 3 E reveal that enrichment of appearing Spp1 peaks at Mer2 sites is abolished in the Spp1CxxCΔ, H3R2A, and H3K4R mutants. Deleting the PHD finger domain of Spp1 eliminates ~75% of appearing Spp1 peaks (264/1,021) detected in wild-type cells; however, about half of the remaining Spp1PHDΔ sites (130 peaks) still exhibit significant enrichment at Mer2 sites. This is in contrast to the Spp1CxxCΔ binding sites and the effects of H3R2A/K4R mutations that apparently prevent enrichment of Spp1 at Mer2 sites. For comparison, we also analyzed the association of the dynamic clusters of Bre2 binding sites defined by cluster analysis (similarly to Spp1 sites) with Mer2 sites. Clearly the appearing Bre2 binding sites are particularly low in Mer2 signal (Fig. 3 E, right panel).

Together, these results further strengthen the tethered loop axis model of meiotic DSB formation proposing that proper localization of Spp1 to chromosome axial sites requires (1) the Mer2-binding (CxxC) motif of Spp1; (2) to a lesser extent, the PHD finger domain; and (3) the presence of histone modifications and modifiable residues (H3K4me3 and H3R2me2s). Consistent with our ChIP-seq data in H3R2/K4 mutants (Fig. 3 E), Spp1 chromatin binding show a global decrease over Mer2 axial sites in set1Δ cells (Fig. S2 C; microarray dataset is from Adam et al., 2018), suggesting that the activity of Set1 is a prerequisite for the full binding of Spp1 to chromatin.

We next examined meiotic chromosome spreads on the colocalization of Spp1 and Mer2 in H3R2 and H3K4 mutants. Unexpectedly, microscopic inspection of Spp1-myc and Mer2-HA.int foci did not show a significant decrease in the number of colocalized spots for H3R2 and H3K4 mutants (Fig. S2 D), in contrast to the reduced ChIP enrichment of Spp1 at axial sites in the same mutants and in set1Δ cells (Fig. 3 and Fig. S2 C). This result indicates that the colocalization, reflecting an apparent interaction of Spp1 with Mer2, is apparently insufficient to promote stable chromatin binding of Spp1 to chromosome axial sites. In the absence of H3R2/K4 methylation, the affinity of Spp1 to chromatin (measured by ChIP enrichment) may decrease significantly and may thus reduce the association of Spp1 with chromatin axial sites. Therefore, we conclude that both Set1-mediated histone methylation and modifiable histone residues are important for the effective binding of Spp1 to the chromosome axis.

Dynamics of Spp1 is influenced by the kinetics of meiotic gene expression

Meiosis involves ~70% of the genes showing a constant transcriptional level, but 30% are regulated up or down (Primig et al., 2000; Borde et al., 2009; Lardenois et al., 2011; Yamaguchi et al., 2012). H3K4me3 and Set1 occupancy have been shown to be increased at the 5'-end of coding regions and correlate with the level of transcription (Ng et al., 2003; Luciano et al., 2017). We therefore asked whether the differential dynamics of Spp1 and Bre2 correlate with the transcriptional level of flanking genes (data are from Brar et al., 2012). We classified protein coding genes into three categories that are associated with Spp1-only, Bre2-only, and common (Bre2 and Spp1) peaks (Fig. 4 A and Fig. S2 B). Based on the median mRNA expression levels, ORFs linked to common (Spp1 and Bre2) sites showed significantly higher transcription rate than Spp1-only and Bre2-only genes (ANOVA with Tukey HSD; P < 0.0001). Intensive transcription at common (Spp1 and Bre2) sites suggests a spatial correlation between the presence of the full Set1 complex over protein coding ORFs and increased mRNA expression levels. This conclusion is also supported by the fact that when we repeated the previous measurement with genes related to dynamic Spp1 binding sites (Fig. 4 B), the smallest and highest mRNA levels have been measured in the appearing and disappearing categories, respectively. It should be also noted that expression of Spp1-associated genes tightly follows the dynamics of Spp1 chromatin binding, since genes in the "appearing" class become rapidly up-regulated, while the "disappearing" class becomes down-regulated in the first few hours of meiosis.

Regarding the chromatin factors that have been implicated in meiotic DSB formation, appearing Spp1 sites show strong association with Mer2 binding sites (Fig. 4 C) with reduced H3K4me3 and Spo11-oligo levels (Fig. 4, D and E), whereas disappearing Spp1 sites are highly enriched in histone H3K4me3 (Fig. 4 D) and Spo11-oligo DSBs (Fig. 4 E) with decreased Mer2 levels (Fig. 4 C). Overall, these results indicate that de novo formed Spp1 binding sites (appearing class) reflect either activated transcription or linkage to axial regions, while loss of Spp1 (disappearing sites) is related to down-regulated/repressed or poised transcription (D'Urso et al., 2016).

Quantitative analysis of Spp1 chromatin binding: estimating effective turnover rates by competition ChIP (c-ChIP)

To quantify the binding characteristics of Spp1 in terms of turnover and residence time, we performed dynamic chromatin mapping using competition c-ChIP, which allowed estimation of turnover rates at Spp1 binding sites (Lickwar et al., 2013; c-ChIP profiles are available through JBrowse, see Materials and methods). We differentially tagged a constitutive and an inducible isoform of SPP1 with 9xmyc and GFP epitopes, respectively (Fig. 5 A) and turned on the expression of the inducible allele

800–2,000 foci were assessed manually for overlap in a total of 10 spread nuclei per time point. Expected random overlaps are represented by dashed lines determined by Monte Carlo simulation (FociSim, see Materials and methods). FociSim mimics random focus distribution based on the assessed parameters: nucleus area, foci numbers, and foci sizes for each nucleus. **(G)** Average Spp1 focus numbers for the meiotic time courses shown in C–F. **(H)** The same as G, except that average Mer2 focus counts are shown. Error bars represent SD.
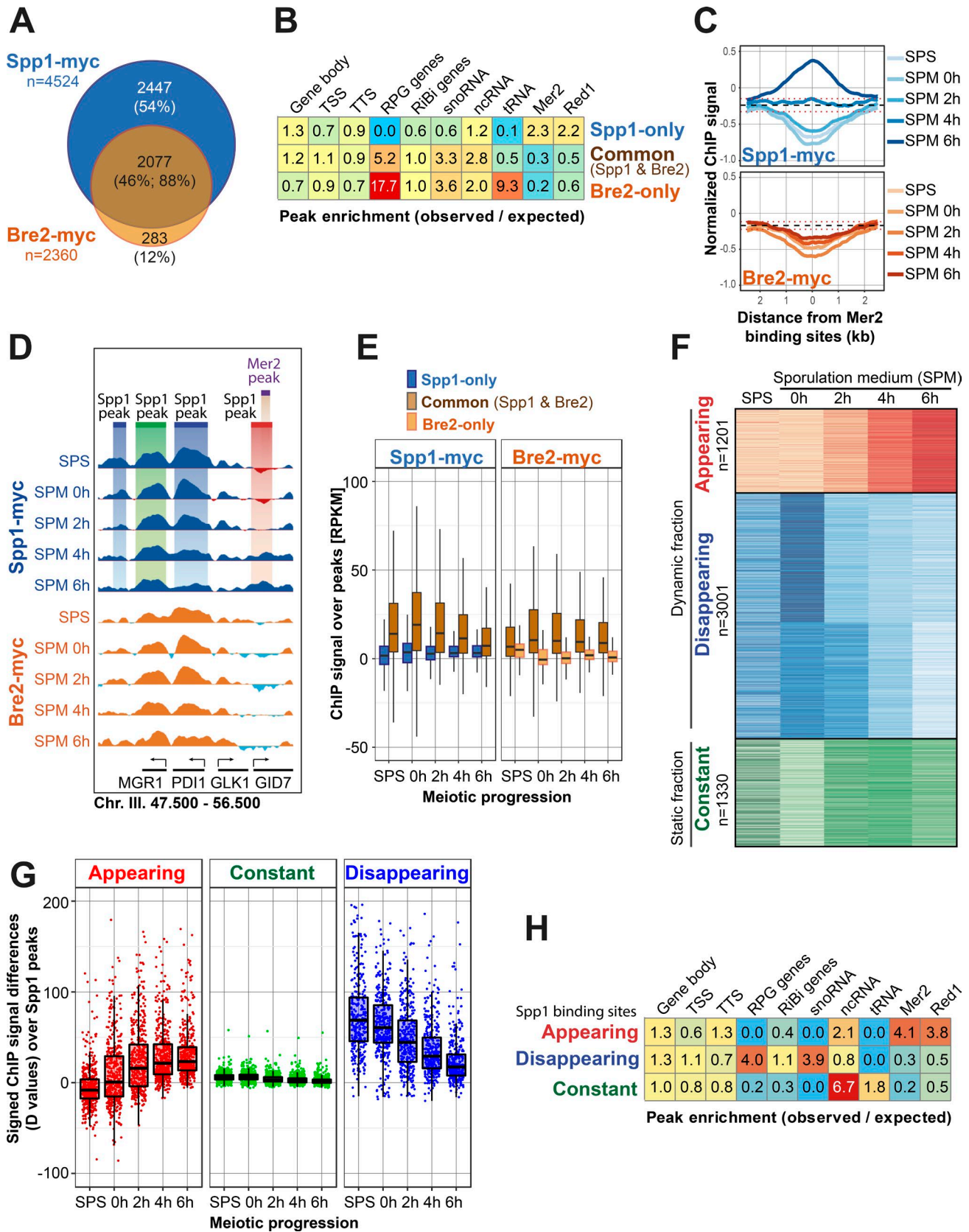
Figure 2. **Chromosomal distribution of Spp1 and Bre2 binding sites during meiotic prophase. (A)** Proportional Venn diagram showing the overlap of Spp1-myc and Bre2-myc binding sites identified in a meiotic time course (SPS; 0, 2, 4, and 6 h in SPM) by ChIP-seq. 54% of Spp1 peaks show no overlap with Bre2, while 88% of Bre2 peaks coincide with Spp1 binding sites. **(B)** Functional annotation of Spp1 and Bre2 sites show differential enrichment over several genomic regions. Spp1-only peaks are highly enriched at chromosome axial sites (Mer2, Red1); common peaks (Spp1 and Bre2) are associated with RPG, snoRNA, and ncRNA genes and depleted over Mer2/Red1 sites; and Bre2-only peaks are enriched at RPG, snoRNA, ncRNA, and tRNA genes and depleted over Mer2/Red1

(driven by a p*CUP1* promoter) with copper addition during the meiotic time course (Fig. S3 A). The level of GFP-Spp1 increased exponentially during the time course and reached its maximum after 6 h in SPM ([Fig. 5 B] and Fig. S3 B). By sampling dense meiotic time points (4.5, 5.0, 5.5, 6.0, and 6.5 h in SPM), both Spp1 isoforms were immunoprecipitated using anti-myc and anti-GFP antibodies, and binding sites were determined according to conventional ChIP-seq pipelines. The resulting Spp1-enriched sites were validated by polar plot comparison of c-ChIP and ChIP peak sets detected at various time points in meiosis (Fig. S3 C). The polar plot shows the highest similarity between the two datasets between 4 and 6.5 h in SPM (dots at the smallest distance from the center, surrounded by a red dashed line), consistent with the c-ChIP experimental design (Fig. S3 A). Then we calculated Spp1 turnover rates by determining the ratio of the GFP (new Spp1) and myc (old Spp1) signals and by fitting the data with an exponential model (Fig. S4 A). Our kinetic model resulted in 977 high confidence peaks that allowed the expression of Spp1 turnover rates as number of Spp1 replacements per unit time (1/min) per genomic region (Fig. S4 B). The analysis shows that Spp1-only sites exhibit different replacement dynamics compared with common (Spp1 and Bre2) binding sites ([Fig. 5 C]). Spp1-only sites move much slower than common (Set1C-associated) sites over gene bodies, transcription termination sites (TTSs), RPG/Ribi genes, and Mer2/Red1 sites (P < 0.001, ANOVA with Tukey HSD). Interestingly, the turnover rate of TSSs is no different between Spp1-only and common peaks (P = 0.181, not significant; ANOVA with Tukey HSD); however, in these genomic regions the highest turnover rates have been measured from all examined regions (P < 0.0001; ANOVA with Tukey HSD). Increased Spp1 mobility in promoter-proximal regions is consistent with the fast turnover of the nucleosomal substrate of Set1C (i.e., H3K4 trimethylated histones; Dion et al., 2007; Kraushaar et al., 2013).

Turnover rate/occupancy plots show that distribution of Spp1 turnover rates only slightly correlates with Spp1 ChIP enrichment (occupancy, R^2 = 0.18; [Fig. 5 D]). However, when Spp1 sites are grouped according to their kinetic behavior (disappearing, appearing, and constant fractions; [Fig. 5 D–H]), the disappearing and emerging Spp1 sites sharply stand apart based on the distribution of turnover rates (disappearing Spp1 sites tend to have higher turnover rates and higher occupancies compared with appearing sites, [Fig. 5 D]). Constant sites are associated with

stochastically distributed values in terms of the above parameters, indicating that a combinatorial action of stably bound and transiently bound Spp1 molecules (present in few cells or large number of cells, respectively) could derive the same apparent ChIP occupancy level. Appearing Spp1 sites exhibit low turnover rates with low Bre2 occupancy ([Fig. 5 E]), low H3K4me3 ([Fig. 5 F]), and high Mer2 enrichment levels ([Fig. 5 G]), whereas disappearing Spp1 sites can be characterized by high turnover rates with high H3K4me3 and Bre2 levels ([Fig. 5, E and F]) and reduced Mer2 occupancies ([Fig. 5 G]). The rate of mRNA expression change of the genes associated with Spp1 negatively correlates with Spp1 turnover rate ([Fig. 5 H]) and sharply separates the kinetic classes of Spp1 binding sites.

From the observed trends, we conclude that (1) turnover rate and occupancy are two measurable properties of the chromatin binding dynamics of Spp1 that effectively discriminates between the different functional types of Spp1 binding sites, (2) differential turnover dynamics of Set1C/Bre2-associated Spp1 sites and Spp1-only sites indicate the presence of two separate Spp1 pools that are characterized by different kinetics and are distributed differently between the Set1 complex and meiotic DSB proteins, and (3) binding of Spp1 to Mer2/Red1 axial sites reduces the rate of Spp1 turnover.

Quantitative microscopic analysis of Spp1 chromatin binding by FRAP and FCS techniques

The c-ChIP approach has superior spatial resolution but its temporal resolving power is relatively low, so we further characterized the nuclear dynamics of Spp1 at an increased temporal resolution. Spp1 and Set1 were tagged with a GFP fluorescent reporter at their N-termini (GFP-Spp1 and GFP-Set1; [Fig. 6 A]) and we measured their mobility in live meiotic cells using fluorescence recovery after photobleaching (FRAP) and fluorescence correlation spectroscopy (FCS). Expression of the fluorescent proteins was controlled by the p*CUP1* promoter by adding 100 µM $CuSO_4$ into the SPM at 0 h. Cells selected for the measurements had a fluorescence intensity well above the background, but were not saturated, which allowed us to stay within the single molecular sensitivity range of FCS (Stasevich et al., 2010).

In the FRAP setting, whole live-cell nuclei were bleached, and fluorescence recovery was recorded in the first 5 h of meiosis ([Fig. 6 B]). GFP-Spp1 and GFP-Set1 reached saturation in <50 s

sites. Heat map shows the overlap ratio of observed and computer randomized binding sites (observed/expected) with the indicated annotation category. **(C)** Spp1-myc is progressively loaded to Mer2 binding sites during meiotic prophase, while the Bre2-myc signal remains depleted throughout the sporulation process. Horizontal dashed line and red dotted lines show the genome-wide average ChIP signal ± SD. **(D)** Representative genome browser snapshot showing the chromosomal distribution of Spp1-myc (blue) and Bre-myc (orange) ChIP signal. Tracks represent meiotic time points. Disappearing, constant, and appearing Spp1 peaks are highlighted in blue, green and red, respectively. A Mer2 site is also shown in purple. **(E)** Common (Spp1 & Bre2) binding sites show increased chromatin association compared with Spp1-only and Bre2-only sites (ANOVA with Tukey HSD; P < 0.0001). Box plots show the distribution of ChIP signals over the three categories (Spp1-only, common, and Bre2-only). Left, Spp1-myc enrichment. Right, Bre2-myc enrichment. **(F)** Temporal classes of Spp1 binding sites identified by cluster analysis. Appearing (red) and disappearing (blue) sites show dynamically increasing/decreasing ChIP enrichment, while constant sites (green) do not show significant temporal changes. Heat maps show the relative changes of ChIP enrichment over time (normalized by rows). **(G)** Confirming the kinetic classes of Spp1 binding sites by an independent approach, based on the absolute values of ChIP enrichments. Spp1 peaks were rank-ordered by their signed ChIP signal differences (D values) between 0 and 6 h in SPM. Sampling the bottom (<q20), middle (q40–q60) and top (>q80) quantiles of the D values recapitulated the dynamic classes of Spp1 sites visualized by cluster analysis (in panel F). **(H)** Functional annotation of the dynamic classes of Spp1 binding sites. Appearing Spp1 peaks are strongly enriched at chromosome axial sites (Red1 and Mer2). Disappearing Spp1 sites are enriched at RPG and snoRNA genes and depleted at Mer2/Red1 sites. Constant Spp1 peaks show strong association with ncRNAs and depletion over Mer2 binding sites. The data are representative of two independent biological replicate experiments. Sample size (n, number of peaks analyzed in each category) is indicated in panels A and F.
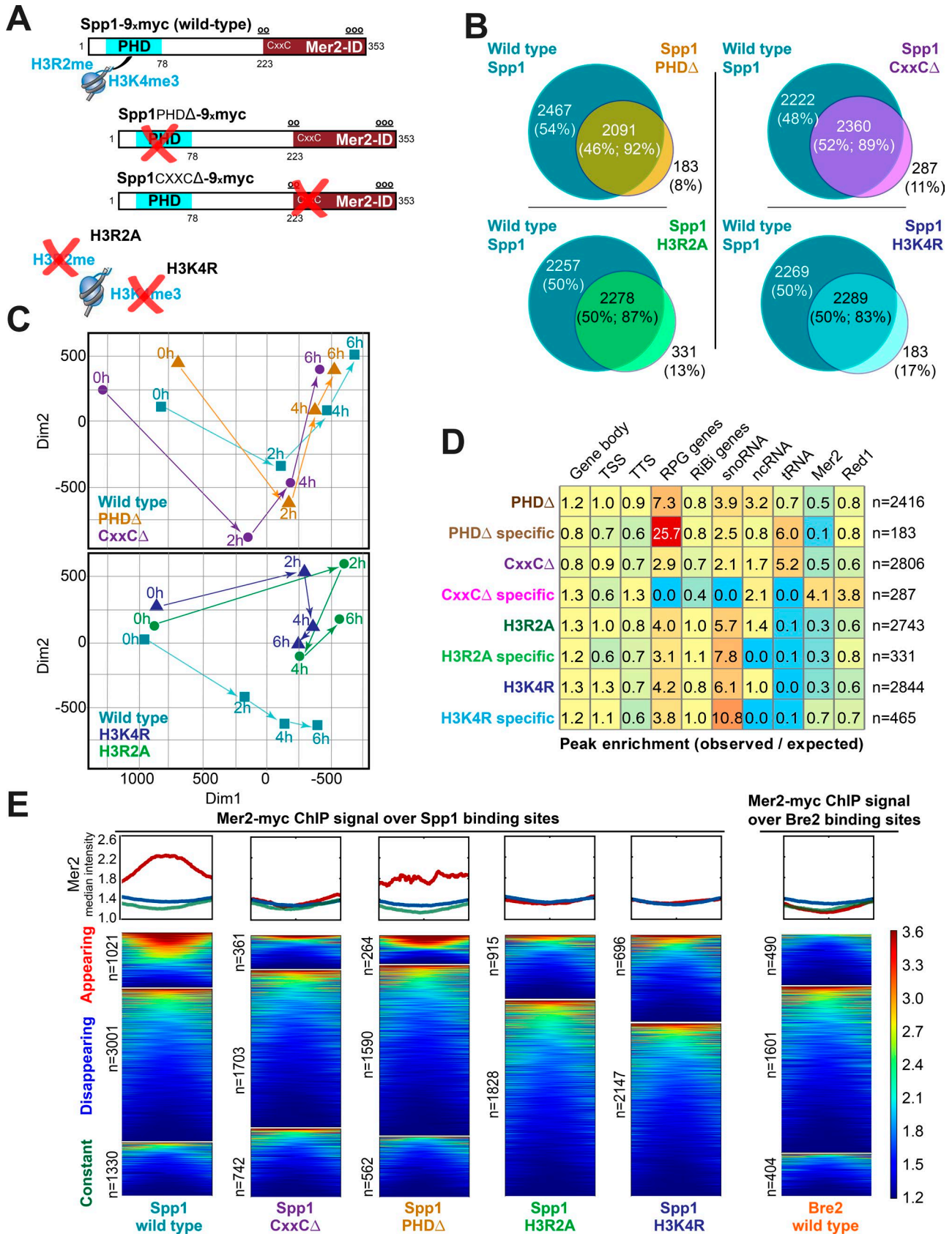
Figure 3. Functional analysis of Spp1 chromosomal binding in meiosis. (A) Schematic structure of the Spp1 mutant proteins studied in ChIP-seq experiments. C-terminal tags are not illustrated. Mutations (highlighted by red Xs) were introduced into the PHD finger domain (blue) and Mer2-interacting motif (brown) of Spp1 and into histone H3R2 and H3K4 (H3R2A and H3K4R). **(B)** Proportional Venn diagram showing the overlap of Spp1 binding sites identified in wild-type and mutant cells during the meiotic time course (0–6 h in SPM). Reduction of Spp1 binding sites for each mutation is indicated on the diagrams.

during recovery, which demonstrates the highly dynamic properties of the mobile fraction of the two molecules. About half of the FRAP signal did not return after the initial bleach pulse, indicating that ~50% of Spp1 and Set1 remain tightly bound to chromatin representing the immobile fraction. The mobile fractions were further characterized by FCS between 0 and 6 h in SPM, allowing us to track the diffusion of one to five molecules at a time (on the scale of milliseconds) within a femtoliter-sized confocal volume. The time-dependent autocorrelation functions were fitted with a 3D normal diffusion model supposing two autonomous diffusing components (ρ_1 and ρ_2; Fig. 6 C), deriving several physicochemical parameters that described the mobility of Set1 and Spp1 (e.g., number of diffusing molecules, diffusion time, diffusion coefficient, and apparent molecular mass). The distribution of fast and slow components did not differ between Spp1 and Set1 (Fig. 6 D, left panel); however, the average diffusion coefficient (D_2) of Spp1 was significantly slower compared with Set1 (Fig. 6 D, middle panel). The changed diffusion coefficient shows the decreased nuclear mobility of Spp1. The average apparent molecular mass of GFP-Set1 (calculated from the Stokes-Einstein equation for spherical objects; Brazda et al., 2014; Hetey et al., 2017) was equal to the expected molecular mass of Set1C (379 kD), while GFP-Spp1 gave ~43-fold higher molecular mass (1,764 kD) than the real molecular mass of the fusion protein, which suggests that Spp1 is attached to a huge macromolecular complex that is different from Set1C (Fig. 6 D, right panel). The large difference between the expected and observed molecular weights of Spp1 cannot be justified by nucleoplasmic interactions with diffusible protein factors alone; instead, transient chromatin associations (e.g., tethering to axial sites) may better explain the differential diffusion behavior of Spp1.

Discussion

Previously, we proposed a model in which the interaction between Spp1 and Mer2 links potential meiotic DSB sites to the chromosome axis, thereby enabling axis-proximal regions that are depleted in nucleosomes to be cut by Spo11 (Acquaviva et al., 2013a,b). However, it remained unknown whether Spp1 was still related to Set1C during this process and whether a specific subpopulation of Spp1 was relocalized from transcribed genes to chromosome axial sites. In addition, the spatial and temporal dynamics of Spp1 redistribution have not been studied so far.

The results presented in this study clearly show that in meiosis Spp1 behaves differently from Set1C/Bre2. This conclusion is

based on the differential chromosomal localization of Spp1 and Bre2, the differential turnover rate dynamics of Spp1 and Set1 binding sites, and the different apparent molecular mass and diffusion coefficient of Spp1 and Set1. Unlike Set1C, the chromatin binding of Spp1 is very dynamic that is characterized by the creation of many new binding sites and the disappearance of many existing binding sites during the first hours of meiotic kinetics. We have shown that dynamic Spp1 sites reflect two populations that bind to chromosome axial sites or highly transcribed genes, respectively. Interestingly, the turnover rate of newly emerging Spp1 binding sites is low, suggesting that prolonged binding of Spp1 to Mer2 might be a prerequisite for DSB selection and formation. Disappearing Spp1 sites were associated with down-regulated genes, indicating that Spp1 might be released from repressed or poised genes similarly to transcriptional memory genes (D'Urso et al., 2016). Disappearing Spp1 binding sites exhibit high turnover rate characteristics and low association with Mer2 binding sites. Interestingly, disappearing Spp1 peaks were predominant at RPG and snoRNA genes that are transiently repressed in the first hours after transfer to SPM (Brar et al., 2012). The mechanism that triggers the dissociation of Spp1 from genomic sites to which Spp1 is tightly bound in rich media needs to be elucidated. Interestingly, the strong association between constant Spp1 peaks and ncRNAs may reflect an unexplored role of Spp1 in regulating noncoding RNA expression. A refined loop axis model (Fig. 7) shows how the dynamic behavior of Spp1 is associated with the different classes of Spp1 binding sites.

Together, our results are consistent with earlier works and further reinforce the tethered loop axis model in the framework of meiotic chromatin structure (Acquaviva et al., 2013b; Sommermeyer et al., 2013; Adam et al., 2018). We demonstrated in our previous work that H3K4me3 is required for Spp1 function, probably by recognizing the PHD-domain of Spp1, and this requirement could be bypassed by artificially tethering Spp1 to a DNA locus. We also reported that the CxxC motif of Spp1 is important for Mer2-Spp1 binding when Spp1 was artificially linked to the $GAL10_{UAS}$ region (Acquaviva et al., 2013b). Our new immunofluorescence experiments with spread meiotic chromosomes clearly show that both Spp1PHDΔ and Spp1CxxCΔ mutations affect the colocalization of Spp1 with Mer2, which usually reaches its maximum by the time of DSBs formation. Therefore, the PHD domain that is located outside the canonical Mer2 domain of Spp1 also contributes to the colocalization of Spp1 and Mer2. This new result is consistent with the genome-wide analysis of Spp1 chromatin binding sites during meiosis, demonstrating

About 90% of Spp1 peaks observed in the mutants overlapped with wild-type Spp1 sites. About 10% of Spp1 peaks formed de novo in the mutants. **(C)** MDS plots visualizing the similarities and differences of Spp1 binding sites identified in wild-type and mutant cells during the meiotic time course (0–6 h in SPM). Each datapoint represents a characteristic Spp1 state specified by cell type and temporal stage in meiosis. Distance of any two datapoints in the MDS map is proportional to the variability of Spp1 states (i.e., Spp1 peak sets). The upper map compares wild-type, Spp1PHDΔ, and Spp1CxxCΔ cells at four meiotic time points (0, 2, 4, and 6 h in SPM). The lower map depicts wild-type, Spp1 H3R2A, and Spp1 H3K4R cells at the same time points. **(D)** Functional annotation of Spp1 binding sites identified in the mutants. Color scale indicates enrichment or depletion within the annotation category. **(E)** Analysis of Mer2 enrichment over the dynamic classes of Spp1 binding sites identified by cluster analysis. Left, Mer2-myc signal enrichment shown on metaplots, centered to Spp1 peak positions identified in wild-type and mutant cells. In wild-type cells, the appearing class of Spp1 binding sites show strong enrichment in Mer2. Dynamic Spp1 clusters are also revealed in the mutants by cluster analysis, however, none of these dynamic sites are associated with Mer2. Right, Mer2-myc signal enrichment over clustered Bre2 chromatin binding sites. The data are representative of two independent biological replicate experiments. Sample size (n, number of peaks analyzed in each category) is indicated in panels B, D, and E.
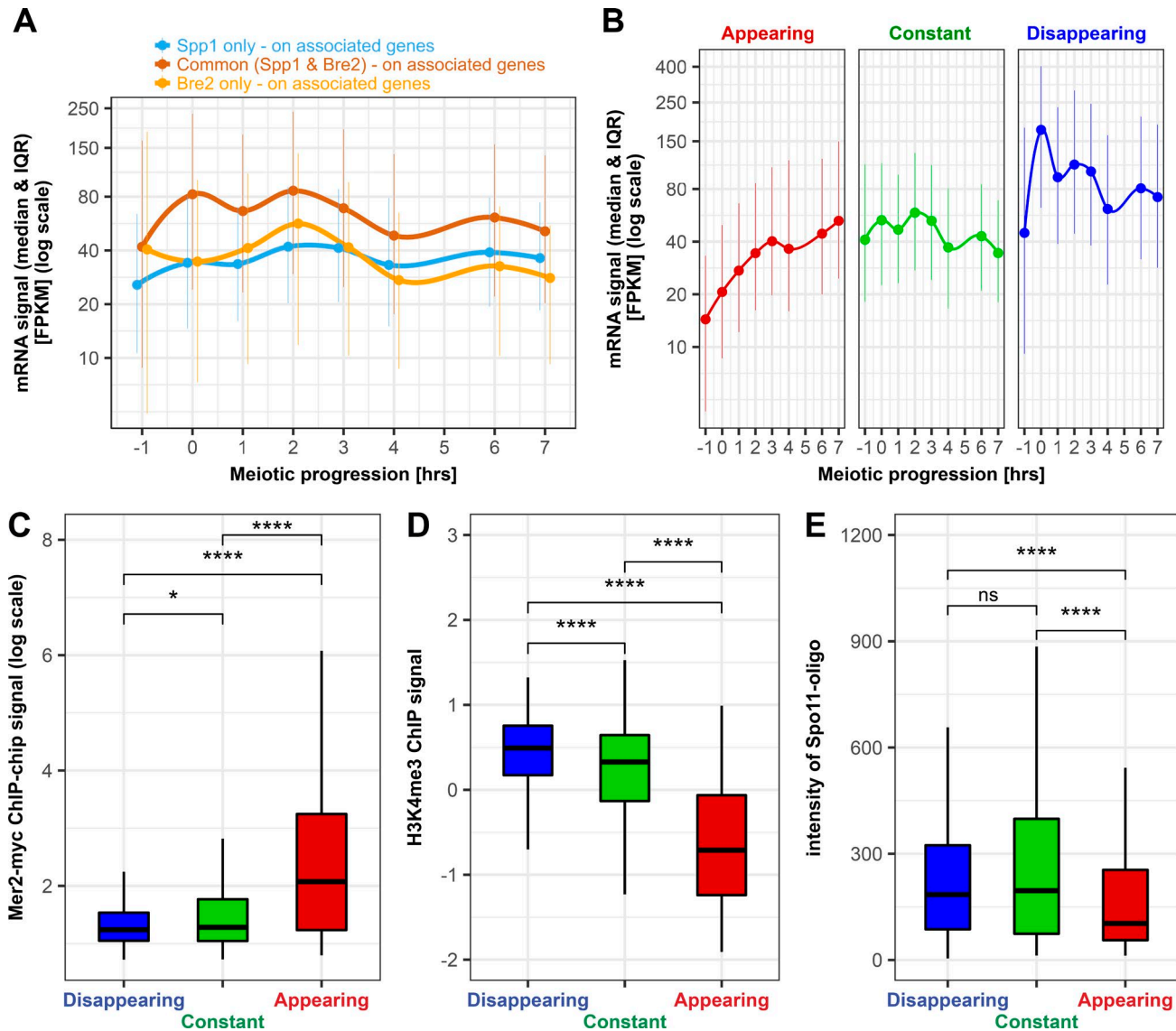
Figure 4. **Spp1 chromatin binding dynamics is influenced by meiotic gene expression. (A)** Spp1-myc and Bre2-myc peaks were assigned to the closest protein coding genes (Fig. S2 B) for which meiotic mRNA levels were determined (data are from Brar et al., 2012) in the three categories of binding sites (Spp1-only, common, and Bre2-only). Median gene expression levels are plotted during the progress of meiotic prophase. Genes associated with both Spp1 and Bre2 show significantly higher expression levels than Spp1-only and Bre2-only genes (ANOVA with Tukey HSD; P < 0.0001). The data are representative of two independent biological replicate experiments. Sample sizes (n): Spp1-only genes (3,479), common genes (1,818), and Bre2-only genes (1,300). **(B)** The mRNA expression level of Spp1-associated genes follows the dynamics of Spp1 chromatin binding. Spp1-myc peaks were assigned to the closest protein coding ORFs, and meiotic mRNA levels were determined (similarly to A). Median mRNA signals (with interquartile ranges) are plotted as a function of meiotic time. Dynamic Spp1 clusters (appearing, constant, and disappearing) that are associated with the flanking genes are highlighted in red, green, and blue. The data are representative of two independent biological replicate experiments. Sample sizes (n, number of associated genes): appearing class (1,043), constant class (1,119), and disappearing class (3,135). **(C–E)** Dynamic classes of Spp1 binding sites show differential enrichment in Mer2 binding (left, data from Panizza et al., 2011), H3K4me3 (middle, data from Borde et al., 2009), and Spo11-oligos (right, data from Mohibullah and Keeney, 2017). Box-whiskers plots show the medians (with interquartile ranges) of Mer2/H3K4me3/Spo11-oligo ChIP signals over Spp1 sites. Statistically significant difference is indicated (Mann-Whitney U test; *, P < 0.05; ****, P < 0.0001; ns, not significant). The data are representative of two independent biological replicate experiments. Sample size (n; number of peaks analyzed in each category): appearing class (464), disappearing class (464), constant class (463).

that Mer2 enrichment in the Spp1CxxCΔ mutant is prevented over newly formed Spp1 peaks and is strongly reduced in the Spp1PHDΔ mutant. These functional data point toward the importance of the PHD and CxxC motifs for the relocation of Spp1. Interestingly, when the H3R2 and H3K4 side chains were mutated to H3R2A and H3K4R, binding of Spp1 to axial sites was compromised, while Spp1 was still able to colocalize with Mer2.

This result indicates that (microscopic) colocalization of Spp1 and Mer2 is not sufficient to promote stable binding of Spp1 to chromatin axial sites and that the PHD domain of Spp1 contributes to the interaction of Spp1 and Mer2 in addition to mediating association with methylated H3R2 and H3K4. One possible interpretation of these results is that the enrichment of Spp1 at Mer2 chromatin binding sites requires both protein–protein
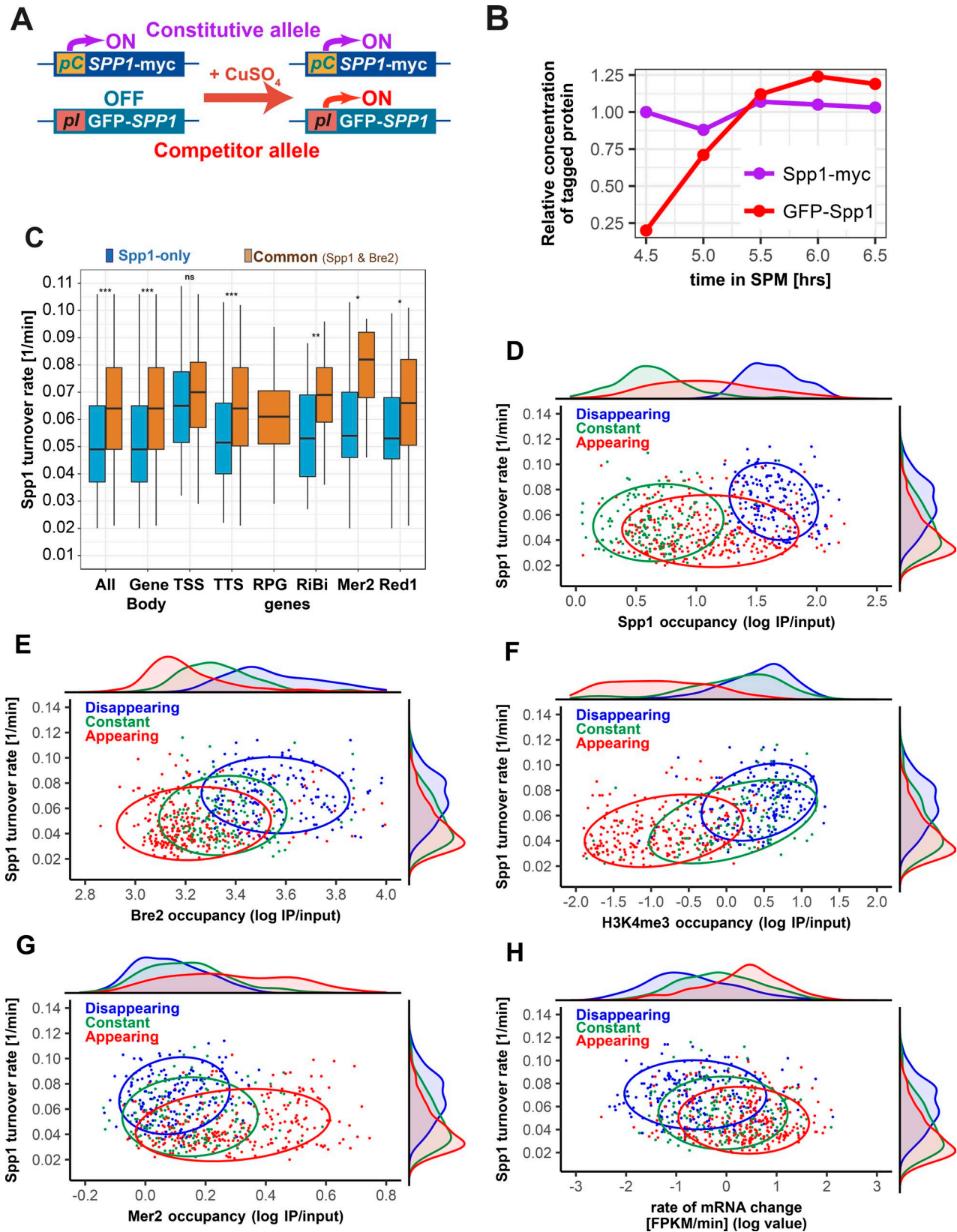
Figure 5. **Competition ChIP unravels turnover rates of Spp1 chromatin binding. (A)** Scheme of the c-ChIP yeast strain. Differentially tagged Spp1 isoforms are expressed from allelic positions in a diploid cell. The constitutive allele (Spp1-myc) is driven by an endogenous *SPP1* promoter while the inducible allele (GFP-Spp1) is controlled by a copper-inducible (p*CUP1*) promoter. Expression of GFP-Spp1 is induced by addition of 200 μM CuSO₄. **(B)** Relative protein levels of induced GFP-Spp1 and constitutive Spp1-myc as a function of time. Copper induction was initiated at 4.5 h in SPM and cells were collected in every 30 min until 6.5 h in SPM to perform Western blot and c-ChIP analyses. The data were obtained from two biological replicate experiments. The graph is representative of the quantitative Western blot measurement shown in Fig. S3 B. **(C)** Turnover rate of Spp1 determined at functional elements of the yeast genome. Spp1-only

interactions between Spp1 and Mer2 and former association of Spp1 with methylated H3R2/K4. The question remains open as to whether H3R2 is directly involved in the recognition of the Spp1 PHD motif. It is noteworthy that half of the remaining appearing peaks of the Spp1PHDΔ mutant still overlap Mer2 binding sites, indicating that the Spp1 PHD domain is not an absolute prerequisite. Notwithstanding, Set1-mediated H3K4 methylation might be important for the relocation and Mer2-association of Spp1 (from loops to axes). It should be also noted that loop-tethering to axial sites may be still possible through diffusion driven (random) processes irrespective of H3K4 methylation and Set1; however, this must be far less effective than the general mechanism that is facilitated by Set1, H3K4me3, modifiable histone residues, and to a lesser extent, the H3K4me3-reader PHD finger motif of Spp1.

We previously demonstrated that the Spp1PHDΔ and Spp1CxxCΔ mutations result in decreased DSB formation at the *BUD23* and *CYS3* recombination hot spots (Acquaviva et al., 2013b). Therefore, we propose that local changes in Spp1 turnover status is determinative for downstream biochemical events governing DNA break and crossover formation. Further studies will be needed to understand the functional implications of Spp1 turnover rate on the distribution of meiotic recombination initiation events. It will be particularly interesting to clarify whether higher Spp1 residence times stimulate the loop-tethering process and thus increase the likelihood of Spo11-mediated cleavage at recombination hot spots.

Materials and methods

Yeast strains

All yeast strains are from the SK1 background and are summarized in Table S1. For sporulation, cells were grown in rich medium (YPD) for 24 h, then transferred to SPS and grown overnight to a density of ~4 × 10^7 cells/ml. Cultures were harvested by centrifugation, washed with one volume of prewarmed 1% potassium acetate and resuspended in SPM (1% potassium acetate supplemented with amino acids and nucleotides according to auxotrophic requirements, and 0.0001% of polypropylene glycol 2000 as an anti-clumping agent) at a density of 2 × 10^7 cells/ml, at 30°C. Meiotic progression and sporulation efficiency was monitored by FACS and fluorescent microscopy of DAPI-stained nuclei. Aberrantly slow or asynchronous sporulation time courses were excluded from further experiments. Spore viability was assessed by tetrad dissection, and it was greater or equal to 90% for all the strains involved in this study.

Chromatin spreads and colocalization statistics

Yeast chromosome spreads were prepared as described (Xaver et al., 2013). Spread nuclei were stained by anti-myc 9E10 mouse antibody (1:50), followed by anti-mouse cy3-conjugated secondary antibody (Jackson ImmunoResearch, 1:400) for Spp1-myc or Bre2-myc, and with rabbit anti-HA antibody (Sigma, 1:100) followed by anti-rabbit FITC-conjugated antibody (Sigma, 1:500) for Mer2-HA. Immunostained, fixed chromosome spreads were analyzed on a ZEISS AXIO Imager M2, with a ZEISS Plan-Neofluar 100×, aperture: 1.3, and a 2× additional magnification by a Zeiss optovar. Specimens were mounted in Vectashield with 0.2 µg/ml DAPI, and well-spread nuclei were selected based on their DNA-morphology (DAPI). Images were taken at a constant exposure time of 2 s for DAPI (BFP channel), CY3 (CY3 channel), and FITC (FITC channel). Light source: Sola SM II (Lumencor); camera: CoolSNAP HQ2 (Visitron Systems GmbH); acquisition software: Visiview (Visitron Systems GmbH). From these records, the nuclear area, foci numbers and foci areas were determined using Fiji software. Signals were counted as overlaps if foci overlapped by >60% of their diameter.

Pictures were optimized for display using linear operations on complete images

To assess the significance of number of Spp1-Mer2 foci overlaps, we performed Monte Carlo simulations (Kurzbauer et al., 2012) of the same foci counts, as well as the same nuclear area and representative foci sizes as measured. Simulated foci were circles which were fully contained within the nuclear ellipse, and overlaps between two foci were counted whenever the pairwise Euclidian distance (d) between their midpoints were smaller than the sum of their radii; i.e., $d(m1, m2) < r1 + r2$, where $m1$ and $m2$ are the midpoints of focus 1 and 2, and $r1$ and $r2$ represent the radii. Each nucleus simulation was repeated 200,000× for assessment of mean expectations and quantiles with high precision. For example, if the experimental overlap was greater than the 0.99 percentile of the simulation, the overlap was judged significant at level $P = 0.01$. Simulated random overlaps were added to each panel shown in Fig. 1 (C–F). For pairwise comparisons between mean values, Welch's *t* test (R, v3.4.3, stats package) was used to calculate significance. Colocalization is presented as overlaps/(all Spp1 foci). This representation can demonstrate changes in the overlap between Spp1 and Mer2 independent of Spp1 foci reduction seen in CxxCΔ, PHDΔ.

FRAP

FRAP measurements were performed in sporulating yeast cells (between 0 and 6 h in SPM) using an Olympus FluoView 1000

---

sites are shown is blue, while common sites (Spp1 and Bre2) are shown in light brown. Turnover of Spp1-only sites is significantly slower compared with common sites (ANOVA with Tukey HSD; *, p ≤ 0.05; **, p ≤ 0.01; ***, p ≤ 0.001; ns, not signficant). Spp1-only peaks were not detected over RPG genes; therefore, turnover rate estimation is missing for this category. **(D–G)** Turnover rate/occupancy plots showing the binding dynamics of Spp1 over Spp1 peaks (D), Bre2 peaks (E), H3K4me3-enriched regions (F), and Mer2 binding sites (G). Disappearing, appearing, and constant kinetic classes are highlighted in blue, red, and green. y axis: Spp1 turnover rate; x axis: occupancy (ChIP enrichment) of Spp1, Bre2, H3K4me3, and Mer2 sites, respectively. Circles comprise the confidence interval (q5–q95) of pointscatter distributions. The measured parameters are also highlighted as histograms (on the top of and right side of scatter plots), showing the distribution of turnover rates and occupancies, respectively. **(H)** Relationship of Spp1 turnover rate and meiotic gene expression rate. Spp1 peaks were assigned to the closest protein coding ORFs and meiotic mRNA levels were determined for each gene (similarly to Fig. 4 B). Spp1 turnover rates (y axis) were plotted in terms of the rate of mRNA change (x axis). Change of transcription rates were computed from the slope of mRNA expression curves (Fig. 4 B) fitted with the least squares method. The data were obtained from two biological replicate experiments. Sample size (n): appearing (286), disappearing (192), and constant (193).
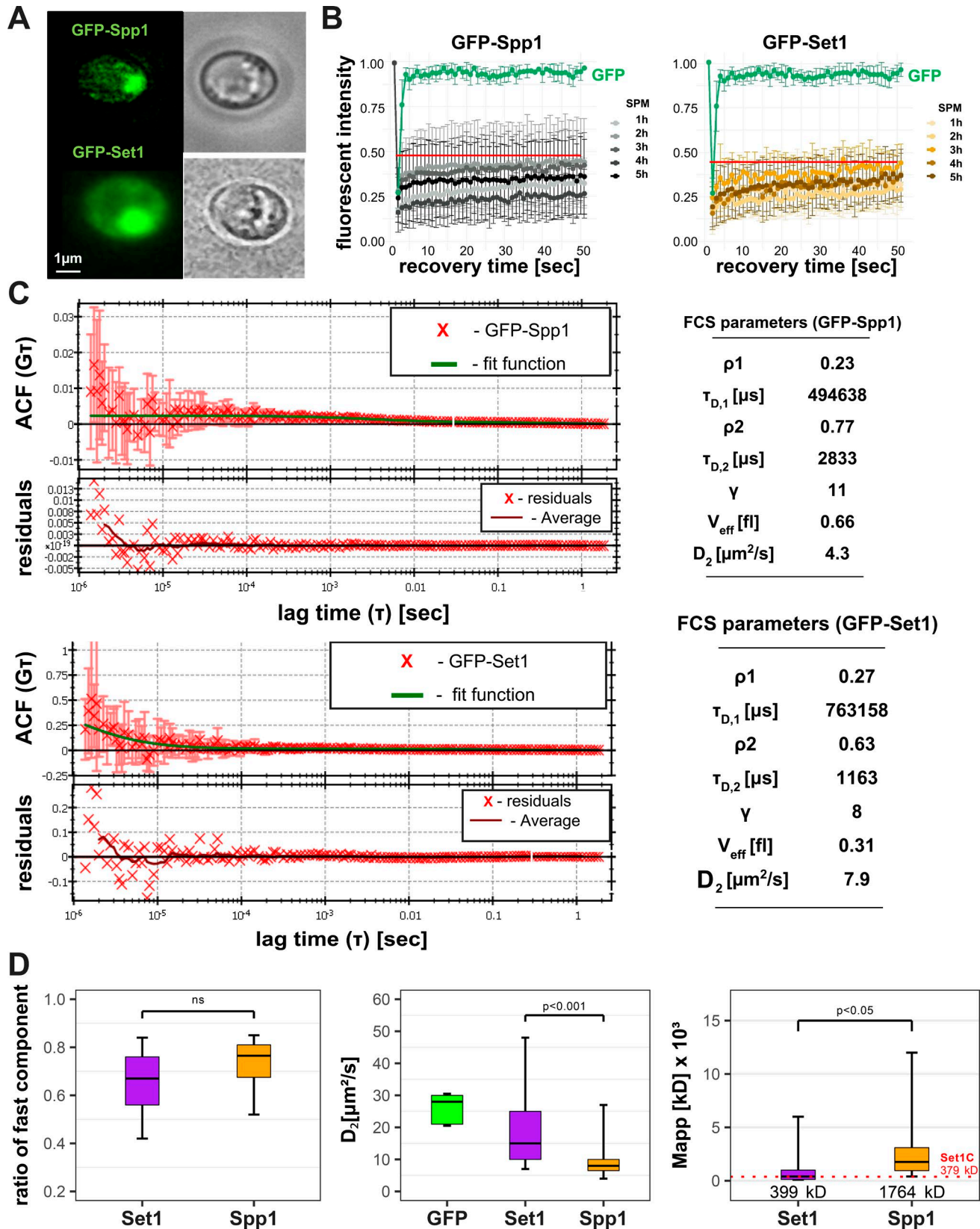
Figure 6. **Quantitative microscopic analysis of Spp1 chromatin binding dynamics based on photobleaching and fluorescence fluctuation. (A)** N-terminally tagged fluorescent Spp1 and Set1 proteins were induced in sporulating yeast cells (between 0 and 5 h in SPM) by adding 100 µM CuSO$_4$. Expression was driven by a p*CUP1* promoter. Both proteins were subjected to FRAP and FCS analyses. **(B)** FRAP curves show the retrieval of GFP-Spp1 (gray), GFP-Set1 (yellow), and GFP-only (green) signals at various meiotic time points. Recoveries reach a plateau phase within 50 s. Horizontal red line indicates the mobile fractions. The FRAP data are representative of two independent biological replicate experiments. Sample size (n) was 30–50 cells per meiotic time point. For each cell, five prebleach images were taken followed by a 500 ms bleach period of 100% laser intensity; then, post-bleach images were recorded in every

confocal microscope, based on an inverted IX-81 stand with an UPlanAPO 60× (NA 1.2) water immersion objective. Samples were taken at every hour from standard liquid sporulation cultures (1% potassium-acetate; imaging medium) and measurements were performed at room temperature (22°C) on microscope slides covered with 1% potassium acetate pad. GFP was excited by the 488-nm argon-ion laser line, and fluorescence was detected through a 500–550-nm band-pass filter. Cells expressing the GFP-Set1 or GFP-Spp1 proteins were randomly selected after CuSO$_4$ induction (100 µM) and five prebleach images were taken (256 × 256–pixel area, 15× zoom, and ~9-µW laser power at the objective) followed by a 500-ms bleach period of 100% laser power (900 µW). Images were taken in every second up to 1 min. Image acquisition was performed by the FV10-ASW v1.5 software. Subsequently, the Fiji software was used to select rectangular areas for bleach regions of interest and to quantitate fluorescence recovery.

FCS

FCS measurements were all performed at room temperature (22°C) using an Olympus FluoView 1000 confocal microscope. Sporulating cells from taken at every hour from liquid sporulation (1% potassium acetate; imaging medium) cultures and FCS was performed on microscope slides covered with 1% potassium acetate pad. Fluorescence fluctuations were detected by avalanche photodiodes (Perkin-Elmer) and autocorrelation curves were calculated by an ALV-5000E correlation card (ALV Laser) at three randomly selected points of each nuclei, with 10 × 8 s runs. For FCS data processing and autocorrelation curve fitting the QuickFit 3.0 software was used (Krieger and Langowski, 2015) applying a 3D normal diffusion model for two-component fitting:

$$G(\tau) = \frac{1}{N}\left[\rho_1\left(1 + \frac{\tau}{\tau_1}\right)^{-1}\left(1 + \frac{\tau}{\gamma^2\tau_1}\right)^{-\frac{1}{2}} + \rho_2\left(1 + \frac{\tau}{\tau_2}\right)^{-1}\left(1 + \frac{\tau}{\gamma^2\tau_2}\right)^{-\frac{1}{2}}\right]$$

where τ is the lag time, τ_{tr} is the triplet correlation time, τ_1 and τ_2 are the diffusion times of the fast and slow species, ρ_1 and ρ_2 = 1 − ρ_1 are the fractional amplitudes of the two components, N is the average number of molecules in the detection volume, and γ is the aspect ratio of the ellipsoidal detection volume. Autocorrelation curves distorted by aggregates floating through the focus were excluded from the analysis.

Western blot

Whole cell extracts were prepared from 5 ml cells (4 × 10^7 cells/ml) sampled from the meiotic time course. Cells were lysed in 150 µl of lysis buffer (1.85 M NaOH, 7.5% β-mercaptoethanol at natural pH) and incubated for 10 min on ice. 150 µl of cold 50% trichloroacetic acid was added and incubated for a further 10 min on ice. The precipitated proteins were pelleted, resuspended in 100 µl of 2× Laemmli buffer, and neutralized by adding 5–10 µl of unbuffered 1 M Tris. Separation and blotting were performed according to standard procedures. Spp1-myc and Spp1-GFP proteins were detected using the 9E10 mouse anti-myc (ab56; Abcam) and anti-GFP (ab290; Abcam) primary antibodies and HRP-conjugated goat anti-mouse (1:100,000; Amersham) secondary antibody. Detection was performed by an ECL prime detection system (GE Healthcare).

ChIP and c-ChIP experiments

50 ml of meiotic cells (4 × 10^7 cells/ml) were collected at the indicated time points and cross-linked with 1% formaldehyde for 20 min at room temperature. Formaldehyde was quenched with 125 mM glycine for 5 min at room temperature, and cells were washed three times with ice-cold 1× TBS at pH 7.5 (20 mM Tris-HCl at pH 7.5 and 150 mM NaCl). Cells were resuspended in 500 µl of lysis buffer (50 mM Hepes KOH at pH 7.5, 140 mM NaCl, 1mM EDTA, 1% Triton X-100, 0.1% Na-deoxycholate, and 1 tablet of complete inhibitor cocktail [Roche] in 50 ml solution) and lysed with acid-washed glass beads for 10 min in a FastPrep bead beater machine. Chromatin samples was fragmented to an average size of 300 bp by sonication (Bioruptor; Diagenode). To obtain whole-cell extract, a 50 µl pre-immunoprecipitation (IP) sample was removed and centrifuged at full speed for 10 s to pellet the cell debris (supernatant = whole-cell extract). The rest of the samples were also centrifuged at 12,000 rpm (4°C) for 20 s to pellet the cell debris. IP was performed by adding the 450-µl extract to a pellet of magnetic protein G dynabeads (Dynal), corresponding to 50 µl or 2 × 10^7 beads, which were preincubated with the 9E11 (monoclonal mouse anti-myc, ab56; Abcam) or anti-GFP (polyclonal rabbit, ab290; Abcam) antibodies overnight at 4°C. IP samples were washed twice with lysis buffer, twice with lysis buffer plus 360 mM NaCl, twice with washing buffer (10 mM Tris-HCl at pH 8.0, 250 mM LiCl, 0.5% NP-40, 0.5% Na-deoxycholate, and 1 mM EDTA), and finally once with 1× TE at pH 7.5, using the magnetic device supplied by Dynal. After reversal of cross-linking by heating in TE-1% SDS overnight at 65°C, the proteins were digested with proteinase K (12 µl of 20 mg/ml stock) for 3h at 65°C. Nucleic acids were PCR clean up kit purified and

second up to 1 min. **(C)** Measuring the diffusional properties of GFP-Spp1 and GFP-Set1 by FCS. Representative time-dependent autocorrelation curves with the estimated diffusion parameters and residuals are shown. FCS curves were fitted with a two-component 3D normal diffusion model. ρ1: slow component; ρ2: fast component; $\tau_{D,1}$: diffusion time of slow component; $\tau_{D,2}$: diffusion time of fast component; γ: structure factor of the confocal volume; V_{eff}: effective measurement volume; D_2: diffusion coefficient of the rapid component in µm^2/s unit. **(D)** Evaluation of the recorded autocorrelation curves show significant differences between GFP-Spp1 and GFP-Set1 diffusion coefficients (D) and apparent molecular mass (M_{app}) with similar fast component distribution. Left, average fraction of fast components after two-component fitting. ns, no statistically significant difference between GFP-Spp1 and GFP-Set1. Middle, distribution of diffusion coefficients. Significant difference is indicated (Mann-Whitney U test). Right, distribution of apparent molecular masses (M_{app}) of the mobile complexes comprising GFP-Spp1 and GFP-Set1. Numbers show median M_{app} values (kD). Significant difference is indicated (Mann-Whitney U test). Molecular mass of the full Set1 complex (red dotted line) is also shown on the right side of the cartoon. The FCS data are representative of two independent biological replicate experiments. Sample size (n) represents 10–40 randomly selected cells.
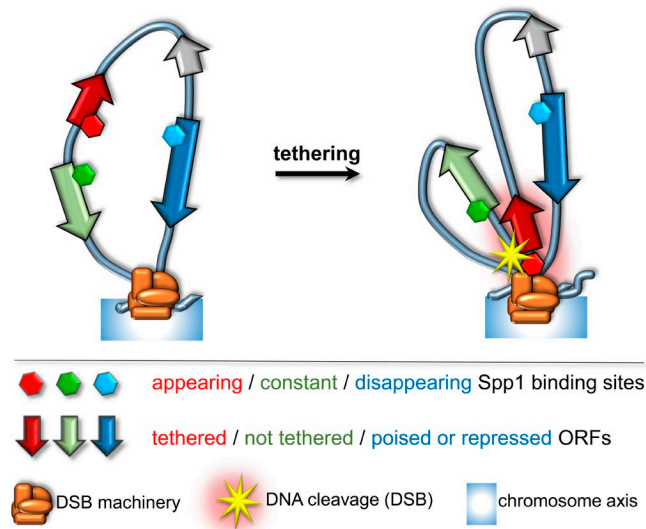
Figure 7. **Loop-axis model showing the dynamic behavior of Spp1 upon tethering.** A subset of Spp1 binding sites (red hexagons) becomes tethered to the chromosome axis (ORFs in red). These tethered sites correspond to the dynamic fraction of Spp1 peaks identified by time resolved ChIP-Seq. Appearing Spp1 sites have the ability to interact with Mer2 and to tether DSB sites to the axis where they undergo Spo11-mediated DNA cleavage (yellow star). These properties depend on the PHD domain and the Mer2 binding motif of Spp1, as well as H3K4 and H3R2 methylation. Constant Spp1 sites (green hexagons) remain unchanged during the meiotic time course. Constant Spp1 sites do not interact with Mer2 and remain colocalized with Set1C (ORFs in green). Disappearing Spp1 sites (blue hexagons) are mainly associated with RPG and SnoRNA genes (ORFs in blue). Spp1 tends to be released from the Set1 holocomplex at the latter sites, reflecting the plasticity of Set1C.

RNA digestion (10 µg RNase) was performed for 1 h at 37°C. The DNA was finally resuspended in 50 µl nuclease-free dH2O.

NGS library preparation and deep sequencing
Sequencing libraries were prepared according to the Illumina's TruSeq ChIP Sample Preparation protocol. In brief, the enriched ChIP DNA was end-repaired and indexed adapters were ligated to the inserts. Purified ligation products were then amplified by PCR. Amplified libraries were prepared in the Genomic Medicine and Bioinformatics Core Facility of the University of Debrecen, Debrecen, Hungary (Halász et al., 2017). The libraries were sequenced using 50 single-end reads with Illumina HiScan SQ (Genomic Medicine and Bioinformatics Core Facility of the University of Debrecen); or with Illumina HiSeq 2500 (EMBL Genomics Core Facility, Heidelberg, Germany).

Raw reads were aligned to the *S. cerevisiae* reference genome (SacCer3; SGD) using the default parameters of Burrows-Wheeler Aligner algorithm (Li and Durbin, 2009) and 38–67% of the sequenced reads were retained after removing low mapping quality (MAPQ < 10) and PCR duplicate reads (Picard).

Enrichment analysis and peak annotation
BayesPeak was used with default parameters to identify ChIP enriched regions (peaks) of the genome compared with input control (Cairns et al., 2011). Peaks sets identified at individual meiotic time points (SPS, 0, 2, 4, and 6 h in SPM) were concat-

enated and sorted by chromosomal position, and then merged. We used mergeBed (Bedtools; Quinlan and Hall, 2010) to join the overlapping peak positions. The overlap of peak sets detected in different samples was represented by proportional Venn diagrams (Larsson, 2018).

We used deepTools2 (Ramírez et al., 2014) bamCoverage to create Reads Per Kilobase per Million mapped reads (RPKM)–normalized bedgraph files. For each bedgraph we calculated the $\log_2$(IP/INPUT) ratios and used these coverage files for visualization and downstream analysis. Heat maps were generated with computeMatrix and plotHeatmap functions of deepTools2. Read density profiles were generated using HOMER (Li et al., 2009) and plotted in R.

To estimate the enrichment or depletion of Spp1 binding sites within genomic features we created 100–100 randomized peak sets with the shuffleBed Bedtools function (Quinlan and Hall, 2010). Then, we calculated with intersectBed the coverage ratio of observed and randomized peak sets over the relevant annotation categories and over Mer2/Red1 ChIP binding sites. Differences in overlap ratios were then compared by the prop. test function of R.

Identification of dynamic Spp1 clusters
To classify Spp1 binding sites based on their binding dynamics, we first merged every Spp1 binding sites identified at all meiotic time points (union peak set). Next, we mapped the average $\log_2$(IP/INPUT) RPKM ratios of the ChIP samples back to the union peak set. Binding site coverage values were z-transformed across ChIP samples with the scale function in R. Dynamic clusters were identified using a k-means algorithm and plotted with pheatmap (Kolde, 2015).

MDS
Using the union peak set as described above, we applied the cmdscale MDS method in R to visualize the level of similarity between Spp1 datasets. Euclidean distance matrices generated from this table were readily used as an input for cmdscale. The resulting 2D coordinates were plotted in R as a scatter plot.

Turnover rate estimation from c-ChIP data
Average coverage (i.e., the occupancy) of the Spp1 binding sites were calculated using both the GFP- and myc competition ChIP-seq data for each time point separately. Next, GFP/myc occupancy ratios were calculated and the same exponential model was fitted as in Deal et al. (2010):

$$\frac{GFP}{myc} = 1 - e^{-\lambda t}$$

where $\frac{GFP}{myc}$ is the GFP/myc occupancy ratio, e is the mathematical constant ~2.72, t is the time measured from the induction of the GFP-tagged *SPP1* allele (in minutes), and λ is the turnover rate (1/min). This model is identical to the one used by others (Dion et al., 2007; Lickwar et al., 2012). After fitting the model, we estimated the standard error of the estimates and performed a Student's t test to evaluate the goodness of fit of the model. In total, 977 binding sites could be described with the model (P value < 0.05). To assess the consistency of Spp1 peak sets identified by c-ChIP

and ChIP experiments, we calculated the mean differences of IP signals (ChIP – c-ChIP) for all meiotic time points and depicted the results by polar plots (Fig. S3 C) using the radarchart function of R.

Statistical analysis

All statistical analyses were performed in R (version 3.4.4). Group comparisons were performed by ANOVA (aov() R function). Groups were compared with Tukey's post-hoc test (Tukey HSD R function). If the data did not fit the normal distribution, we used Kruskal-Wallis's ANOVA (kruskal.test R function) and the Mann-Whitney U test (wilcox.test R function). Probability values of $P ≤ 0.001$ were considered as statistically significant. Significance marks: not significant (ns). $P > 0.05$; *, $P ≤ 0.05$; **, $P ≤ 0.01$; ***, $P ≤ 0.001$; ****, $P ≤ 0.0001$. The number of cases (n) and P values were indicated in each legend.

External datasets

SacCer3 genome annotation files were obtained from *Saccharomyces* Genome Database. Promoter and downstream regions were defined as the arbitrary extension of TSSs with 500 bp and TTS by 200 bp. RNA-seq (Brar et al., 2012), H3K4me3 ChIP-chip (Borde et al., 2009), Mer2 and Red1 ChIP-Chip (Panizza et al., 2011; Sun et al., 2015), and Spo11-oligo DSB data (Mohibullah and Keeney, 2017) were from the indicated publications.

Data access

Raw sequencing data and processed data files generated in this study have been deposited to Gene Expression Omnibus (GEO) with the accession no. GSE107967.

ChIP-seq data can be accessed and browsed in JBrowse (http://geneart.med.unideb.hu/pub/2018-spp1; login: spp1; password: cerevisiae7).

Online supplemental material

Fig. S1 reports the meiotic progression and sporulation efficiency of yeast strains analyzed by ChIP sequencing. Fig. S2 shows the overlap analysis and ChIP enrichment of Spp1 binding sites in various mutants analyzed in this study. Fig. S3 outlines the experimental design and validation of competition ChIP experiments. Fig. S4 shows the turnover rate estimation from competition ChIP data. Table S1 summarizes the P values related to microscopic colocalization analysis, lists the yeast strains used in this study, and provides basic NGS statistics for ChIP sequencing experiments.

Acknowledgments

Author contributions: Z. Karányi conceptualized the c-ChIP sequencing experiments, performed, and conducted all bioinformatical and statistical analyses. L. Halász performed bioinformatic analyses (ChIP-seq). L. Acquaviva constructed mutant strains and conceptualized the work. D. Jónás performed bioinformatical analysis (c-ChIP). S. Hetey performed the FCS and FRAP measurements. B. Boros-Oláh performed the ChIP and Western blot experiments. F. Peng constructed strains and performed and analyzed chromosome spread experiments. D. Chen designed and wrote FociSim, a Java program to assess significance of foci colocalization. F. Klein planned and analyzed chromosome spread experiments. V. Géli conceptualized and coordinated the research and wrote the manuscript. L. Székvölgyi conceptualized and coordinated the research, constructed strains, wrote the manuscript, and secured funding.

References

Acquaviva, L., J. Drogat, P.M. Dehé, C. de La Roche Saint-André, and V. Géli. 2013a. Spp1 at the crossroads of H3K4me3 regulation and meiotic recombination. *Epigenetics.* 8:355–360. https://doi.org/10.4161/epi.24295

Acquaviva, L., L. Székvölgyi, B. Dichtl, B.S. Dichtl, C. de La Roche Saint André, A. Nicolas, and V. Géli. 2013b. The COMPASS subunit Spp1 links histone methylation to initiation of meiotic recombination. *Science.* 339:215–218. https://doi.org/10.1126/science.1225739

Adam, C., R. Guérois, A. Citarella, L. Verardi, F. Adolphe, C. Béneut, V. Sommermeyer, C. Ramus, J. Govin, Y. Couté, and V. Borde. 2018. The PHD finger protein Spp1 has distinct functions in the Set1 and the meiotic DSB formation complexes. *PLoS Genet.* 14:e1007223. https://doi.org/10.1371/journal.pgen.1007223

Battaglia, S., M. Lidschreiber, C. Baejen, P. Torkler, S.M. Vos, and P. Cramer. 2017. RNA-dependent chromatin association of transcription elongation factors and Pol II CTD kinases. *eLife.* 6:1–26. https://doi.org/10.7554/eLife.25637

Baudat, F., J. Buard, C. Grey, A. Fledel-Alon, C. Ober, M. Przeworski, G. Coop, and B. de Massy. 2010. PRDM9 is a major determinant of meiotic recombination hotspots in humans and mice. *Science.* 327:836–840. https://doi.org/10.1126/science.1183439

Borde, V., and B. de Massy. 2013. Programmed induction of DNA double strand breaks during meiosis: setting up communication between DNA and the chromosome structure. *Curr. Opin. Genet. Dev.* 23:147–155. https://doi.org/10.1016/j.gde.2012.12.002

Borde, V., N. Robine, W. Lin, S. Bonfils, V. Géli, and A. Nicolas. 2009. Histone H3 lysine 4 trimethylation marks meiotic recombination initiation sites. *EMBO J.* 28:99–111. https://doi.org/10.1038/emboj.2008.257

Brar, G.A., M. Yassour, N. Friedman, A. Regev, N.T. Ingolia, and J.S. Weissman. 2012. High-resolution view of the yeast meiotic program revealed by ribosome profiling. *Science.* 335:552–557. https://doi.org/10.1126/science.1215110

Brazda, P., J. Krieger, B. Daniel, D. Jonas, T. Szekeres, J. Langowski, K. Tóth, L. Nagy, and G. Vámosi. 2014. Ligand binding shifts highly mobile retinoid X receptor to the chromatin-bound state in a coactivator-dependent manner, as revealed by single-cell imaging. *Mol. Cell. Biol.* 34:1234–1245. https://doi.org/10.1128/MCB.01097-13

Cairns, J., C. Spyrou, R. Stark, M.L. Smith, A.G. Lynch, and S. Tavaré. 2011. BayesPeak--an R package for analysing ChIP-seq data. *Bioinformatics.* 27:713–714. https://doi.org/10.1093/bioinformatics/btq685

D'Urso, A., Y.H. Takahashi, B. Xiong, J. Marone, R. Coukos, C. Randise-Hinchliff, J.-P. Wang, A. Shilatifard, and J.H. Brickner. 2016. Set1/COMPASS

and Mediator are repurposed to promote epigenetic transcriptional memory. *eLife.* 5:e16691. https://doi.org/10.7554/eLife.16691

Daniel, J.A., M.A. Santos, Z. Wang, C. Zang, K.R. Schwab, M. Jankovic, D. Filsuf, H.-T. Chen, A. Gazumyan, A. Yamane, et al. 2010. PTIP promotes chromatin changes critical for immunoglobulin class switch recombination. *Science.* 329:917–923. https://doi.org/10.1126/science.1187942

Deal, R.B., J.G. Henikoff, and S. Henikoff. 2010. Genome-wide kinetics of nucleosome turnover determined by metabolic labeling of histones. *Science.* 328:1161–1164. https://doi.org/10.1126/science.1186777

Dehé, P.-M., B. Dichtl, D. Schaft, A. Roguev, M. Pamblanco, R. Lebrun, A. Rodríguez-Gil, M. Mkandawire, K. Landsberg, A. Shevchenko, et al. 2006. Protein interactions within the Set1 complex and their roles in the regulation of histone 3 lysine 4 methylation. *J. Biol. Chem.* 281:35404–35412. https://doi.org/10.1074/jbc.M603099200

Dion, M.F., T. Kaplan, M. Kim, S. Buratowski, N. Friedman, and O.J. Rando. 2007. Dynamics of replication-independent histone turnover in budding yeast. *Science.* 315:1405–1408. https://doi.org/10.1126/science.1134053

Ernst, P., and C.R. Vakoc. 2012. WRAD: enabler of the SET1-family of H3K4 methyltransferases. *Brief. Funct. Genomics.* 11:217–226. https://doi.org/10.1093/bfgp/els017

Gothwal, S.K., N.J. Patel, M.M. Colletti, H. Sasanuma, M. Shinohara, A. Hochwagen, and A. Shinohara. 2016. The double-strand break landscape of meiotic chromosomes is shaped by the Paf1 transcription elongation complex in Saccharomyces cerevisiae. *Genetics.* 202:497–512. https://doi.org/10.1534/genetics.115.177287

Halász, L., Z. Karányi, B. Boros-Oláh, T. Kuik-Rózsa, É. Sipos, É. Nagy, Á. Mosolygó-L, A. Mázló, É. Rajnavölgyi, G. Halmos, and L. Székvölgyi. 2017. RNA-DNA hybrid (R-loop) immunoprecipitation mapping: an analytical workflow to evaluate inherent biases. *Genome Res.* 27:1063–1073. https://doi.org/10.1101/gr.219394.116

Halbach, A., H. Zhang, A. Wengi, Z. Jablonska, I.M.L. Gruber, R.E. Halbeisen, P.-M. Dehé, P. Kemmeren, F. Holstege, V. Géli, et al. 2009. Cotranslational assembly of the yeast SET1C histone methyltransferase complex. *EMBO J.* 28:2959–2970. https://doi.org/10.1038/emboj.2009.240

Hetey, S., B. Boros-Oláh, T. Kuik-Rózsa, Q. Li, Z. Karányi, Z. Szabó, J. Roszik, N. Szalóki, G. Vámosi, K. Tóth, and L. Székvölgyi. 2017. Biophysical characterization of histone H3.3 K27M point mutation. *Biochem. Biophys. Res. Commun.* 490:868–875. https://doi.org/10.1016/j.bbrc.2017.06.133

Keeney, S., C.N. Giroux, and N. Kleckner. 1997. Meiosis-specific DNA double-strand breaks are catalyzed by Spo11, a member of a widely conserved protein family. *Cell.* 88:375–384. https://doi.org/10.1016/S0092-8674(00)81876-0

Kim, J., J.A. Kim, R.K. McGinty, U.T.T. Nguyen, T.W. Muir, C.D. Allis, and R.G. Roeder. 2013. The n-SET domain of Set1 regulates H2B ubiquitylation-dependent H3K4 methylation. *Mol. Cell.* 49:1121–1133. https://doi.org/10.1016/j.molcel.2013.01.034

Kirmizis, A., H. Santos-Rosa, C.J. Penkett, M.A. Singer, M. Vermeulen, M. Mann, J. Bähler, R.D. Green, and T. Kouzarides. 2007. Arginine methylation at histone H3R2 controls deposition of H3K4 trimethylation. *Nature.* 449:928–932. https://doi.org/10.1038/nature06160

Kolde, R. 2015. pheatmap: Pretty Heatmaps. https://cran.r-project.org/web/packages/pheatmap/index.html (accessed May 19, 2018).

Kraushaar, D.C., W. Jin, A. Maunakea, B. Abraham, M. Ha, and K. Zhao. 2013. Genome-wide incorporation dynamics reveal distinct categories of turnover for the histone variant H3.3. *Genome Biol.* 14:R121. https://doi.org/10.1186/gb-2013-14-10-r121

Krieger, J.W., and J. Langowski. 2015. QuickFit 3.0 (status: beta, compiled: 2015-03-18, SVN: 3891): A data evaluation application for biophysics. http://www.dkfz.de/Macromol/quickfit/ (accessed March 18, 2015).

Krogan, N.J., J. Dover, A. Wood, J. Schneider, J. Heidt, M.A. Boateng, K. Dean, O.W. Ryan, A. Golshani, M. Johnston, et al. 2003. The Paf1 complex is required for histone H3 methylation by COMPASS and Dot1p: linking transcriptional elongation to histone methylation. *Mol. Cell.* 11:721–729. https://doi.org/10.1016/S1097-2765(03)00091-1

Kurzbauer, M.T., C. Uanschou, D. Chen, and P. Schlögelhofer. 2012. The recombinases DMC1 and RAD51 are functionally and spatially separated during meiosis in Arabidopsis. *Plant Cell.* 24:2058–2070. https://doi.org/10.1105/tpc.112.098459

Lam, I., and S. Keeney. 2015. Mechanism and regulation of meiotic recombination initiation. *Cold Spring Harb. Perspect. Biol.* 7:a016634. https://doi.org/10.1101/cshperspect.a016634

Lardenois, A., Y. Liu, T. Walther, F. Chalmel, B. Evrard, M. Granovskaia, A. Chu, R.W. Davis, L.M. Steinmetz, and M. Primig. 2011. Execution of the meiotic noncoding RNA expression program and the onset of gameto-

genesis in yeast require the conserved exosome subunit Rrp6. *Proc. Natl. Acad. Sci. USA.* 108:1058–1063. https://doi.org/10.1073/pnas.1016459108

Larsson, J. 2018. eulerr: Area-Proportional Euler and Venn Diagrams with Ellipses. http://lup.lub.lu.se/student-papers/record/8934042 (accessed February 14, 2018).

Li, H., and R. Durbin. 2009. Fast and accurate short read alignment with Burrows-Wheeler transform. *Bioinformatics.* 25:1754–1760. https://doi.org/10.1093/bioinformatics/btp324

Li, H., B. Handsaker, A. Wysoker, T. Fennell, J. Ruan, N. Homer, G. Marth, G. Abecasis, and R. Durbin. 1000 Genome Project Data Processing Subgroup. 2009. The Sequence Alignment/Map format and SAMtools. *Bioinformatics.* 25:2078–2079. https://doi.org/10.1093/bioinformatics/btp352

Lickwar, C.R., F. Mueller, S.E. Hanlon, J.G. McNally, and J.D. Lieb. 2012. Genome-wide protein-DNA binding dynamics suggest a molecular clutch for transcription factor function. *Nature.* 484:251–255. https://doi.org/10.1038/nature10985

Lickwar, C.R., F. Mueller, and J.D. Lieb. 2013. Genome-wide measurement of protein-DNA binding dynamics using competition ChIP. *Nat. Protoc.* 8:1337–1353. https://doi.org/10.1038/nprot.2013.077

Liu, H., S. Takeda, R. Kumar, T.D. Westergard, E.J. Brown, T.K. Pandita, E.H.-Y. Cheng, and J.J.-D. Hsieh. 2010. Phosphorylation of MLL by ATR is required for execution of mammalian S-phase checkpoint. *Nature.* 467:343–346. https://doi.org/10.1038/nature09350

Luciano, P., J. Jeon, A. El-Kaoutari, D. Challal, A. Bonnet, M. Barucco, T. Candelli, F. Jourquin, P. Lesage, J. Kim, et al. 2017. Binding to RNA regulates Set1 function. *Cell Discov.* 3:17040. https://doi.org/10.1038/celldisc.2017.40

Miller, T., N.J. Krogan, J. Dover, H. Erdjument-Bromage, P. Tempst, M. Johnston, J.F. Greenblatt, and A. Shilatifard. 2001. COMPASS: a complex of proteins associated with a trithorax-related SET domain protein. *Proc. Natl. Acad. Sci. USA.* 98:12902–12907. https://doi.org/10.1073/pnas.231473398

Mohibullah, N., and S. Keeney. 2017. Numerical and spatial patterning of yeast meiotic DNA breaks by Tel1. *Genome Res.* 27:278–288. https://doi.org/10.1101/gr.213587.116

Nagy, P.L., J. Griesenbeck, R.D. Kornberg, and M.L. Cleary. 2002. A trithorax-group complex purified from Saccharomyces cerevisiae is required for methylation of histone H3. *Proc. Natl. Acad. Sci. USA.* 99:90–94. https://doi.org/10.1073/pnas.221596698

Ng, H.H., S. Dole, and K. Struhl. 2003. The Rtf1 component of the Paf1 transcriptional elongation complex is required for ubiquitination of histone H2B. *J. Biol. Chem.* 278:33625–33628. https://doi.org/10.1074/jbc.C300270200

Pan, J., M. Sasaki, R. Kniewel, H. Murakami, H.G. Blitzblau, S.E. Tischfield, X. Zhu, M.J. Neale, M. Jasin, N.D. Socci, et al. 2011. A hierarchical combination of factors shapes the genome-wide topography of yeast meiotic recombination initiation. *Cell.* 144:719–731. https://doi.org/10.1016/j.cell.2011.02.009

Panizza, S., M.A. Mendoza, M. Berlinger, L. Huang, A. Nicolas, K. Shirahige, and F. Klein. 2011. Spo11-accessory proteins link double-strand break sites to the chromosome axis in early meiotic recombination. *Cell.* 146:372–383. https://doi.org/10.1016/j.cell.2011.07.003

Parvanov, E.D., P.M. Petkov, and K. Paigen. 2010. Prdm9 controls activation of mammalian recombination hotspots. *Science.* 327:835. https://doi.org/10.1126/science.1181495

Primig, M., R.M. Williams, E.A. Winzeler, G.G. Tevzadze, A.R. Conway, S.Y. Hwang, R.W. Davis, and R.E. Esposito. 2000. The core meiotic transcriptome in budding yeasts. *Nat. Genet.* 26:415–423. https://doi.org/10.1038/82539

Quinlan, A.R., and I.M. Hall. 2010. BEDTools: a flexible suite of utilities for comparing genomic features. *Bioinformatics.* 26:841–842. https://doi.org/10.1093/bioinformatics/btq033

Ramírez, F., F. Dündar, S. Diehl, B.A. Grüning, and T. Manke. 2014. deepTools: a flexible platform for exploring deep-sequencing data. *Nucleic Acids Res.* 42(W1):W187–W191. https://doi.org/10.1093/nar/gku365

Roguev, A., D. Schaft, A. Shevchenko, W.W.M.P. Pijnappel, M. Wilm, R. Aasland, and A.F. Stewart. 2001. The Saccharomyces cerevisiae Set1 complex includes an Ash2 homologue and methylates histone 3 lysine 4. *EMBO J.* 20:7137–7148. https://doi.org/10.1093/emboj/20.24.7137

Rothbart, S.B., and B.D. Strahl. 2014. Interpreting the language of histone and DNA modifications. *Biochim. Biophys. Acta.* 1839:627–643. https://doi.org/10.1016/j.bbagrm.2014.03.001

Ruthenburg, A.J., C.D. Allis, and J. Wysocka. 2007. Methylation of lysine 4 on histone H3: intricacy of writing and reading a single epigenetic mark. *Mol. Cell.* 25:15–30. https://doi.org/10.1016/j.molcel.2006.12.014

Sayou, C., G. Millán-Zambrano, H. Santos-Rosa, E. Petfalski, S. Robson, J. Houseley, T. Kouzarides, and D. Tollervey. 2017. RNA binding by the histone methyltransferases Set1 and Set2. *Mol. Cell. Biol.* 37:e00165-17. https://doi.org/10.1128/MCB.00165-17

Shilatifard, A. 2012. The COMPASS family of histone H3K4 methylases: mechanisms of regulation in development and disease pathogenesis. *Annu. Rev. Biochem.* 81:65–95. https://doi.org/10.1146/annurev-biochem-051710-134100

Soares, L.M., M. Radman-Livaja, S.G. Lin, O.J. Rando, and S. Buratowski. 2014. Feedback control of Set1 protein levels is important for proper H3K4 methylation patterns. *Cell Reports.* 6:961–972. https://doi.org/10.1016/j.celrep.2014.02.017

Sollier, J., W. Lin, C. Soustelle, K. Suhre, A. Nicolas, V. Géli, and C. de La Roche Saint-André. 2004. Set1 is required for meiotic S-phase onset, double-strand break formation and middle gene expression. *EMBO J.* 23:1957–1967. https://doi.org/10.1038/sj.emboj.7600204

Sommermeyer, V., C. Béneut, E. Chaplais, M.E. Serrentino, and V. Borde. 2013. Spp1, a member of the Set1 Complex, promotes meiotic DSB formation in promoters by tethering histone H3K4 methylation sites to chromosome axes. *Mol. Cell.* 49:43–54. https://doi.org/10.1016/j.molcel.2012.11.008

Stasevich, T.J., F. Mueller, A. Michelman-Ribeiro, T. Rosales, J.R. Knutson, and J.G. McNally. 2010. Cross-validating FRAP and FCS to quantify the impact of photobleaching on in vivo binding estimates. *Biophys. J.* 99:3093–3101. https://doi.org/10.1016/j.bpj.2010.08.059

Sun, X., L. Huang, T.E. Markowitz, H.G. Blitzblau, D. Chen, F. Klein, and A. Hochwagen. 2015. Transcription dynamically patterns the meiotic chromosome-axis interface. *eLife.* 4:1–23. https://doi.org/10.7554/eLife.07424

Székvölgyi, L., and A. Nicolas. 2010. From meiosis to postmeiotic events: homologous recombination is obligatory but flexible. *FEBS J.* 277:571–589. https://doi.org/10.1111/j.1742-4658.2009.07502.x

Székvölgyi, L., K. Ohta, and A. Nicolas. 2015. Initiation of meiotic homologous recombination: flexibility, impact of histone modifications, and chromatin remodeling. *Cold Spring Harb. Perspect. Biol.* 7:a016527. https://doi.org/10.1101/cshperspect.a016527

Tessarz, P., and T. Kouzarides. 2014. Histone core modifications regulating nucleosome structure and dynamics. *Nat. Rev. Mol. Cell Biol.* 15:703–708. https://doi.org/10.1038/nrm3890

Trésaugues, L., P.-M. Dehé, R. Guérois, A. Rodriguez-Gil, I. Varlet, P. Salah, M. Pamblanco, P. Luciano, S. Quevillon-Cheruel, J. Sollier, et al. 2006. Structural characterization of Set1 RNA recognition motifs and their role in histone H3 lysine 4 methylation. *J. Mol. Biol.* 359:1170–1181. https://doi.org/10.1016/j.jmb.2006.04.050

Xaver, M., L. Huang, D. Chen, and F. Klein. 2013. Smc5/6-Mms21 prevents and eliminates inappropriate recombination intermediates in meiosis. *PLoS Genet.* 9:e1004067. https://doi.org/10.1371/journal.pgen.1004067

Yamaguchi, S., K. Hong, R. Liu, L. Shen, A. Inoue, D. Diep, K. Zhang, and Y. Zhang. 2012. Tet1 controls meiosis by regulating meiotic gene expression. *Nature.* 492:443–447. https://doi.org/10.1038/nature11709

Yamashita, K., M. Shinohara, and A. Shinohara. 2004. Rad6-Bre1-mediated histone H2B ubiquitylation modulates the formation of double-strand breaks during meiosis. *Proc. Natl. Acad. Sci. USA.* 101:11380–11385. https://doi.org/10.1073/pnas.0400078101

Yuan, C.C., A.G.W. Matthews, Y. Jin, C.F. Chen, B.A. Chapman, T.K. Ohsumi, K.C. Glass, T.G. Kutateladze, M.L. Borowsky, K. Struhl, and M.A. Oettinger. 2012. Histone H3R2 symmetric dimethylation and histone H3K4 trimethylation are tightly correlated in eukaryotic genomes. *Cell Reports.* 1:83–90. https://doi.org/10.1016/j.celrep.2011.12.008
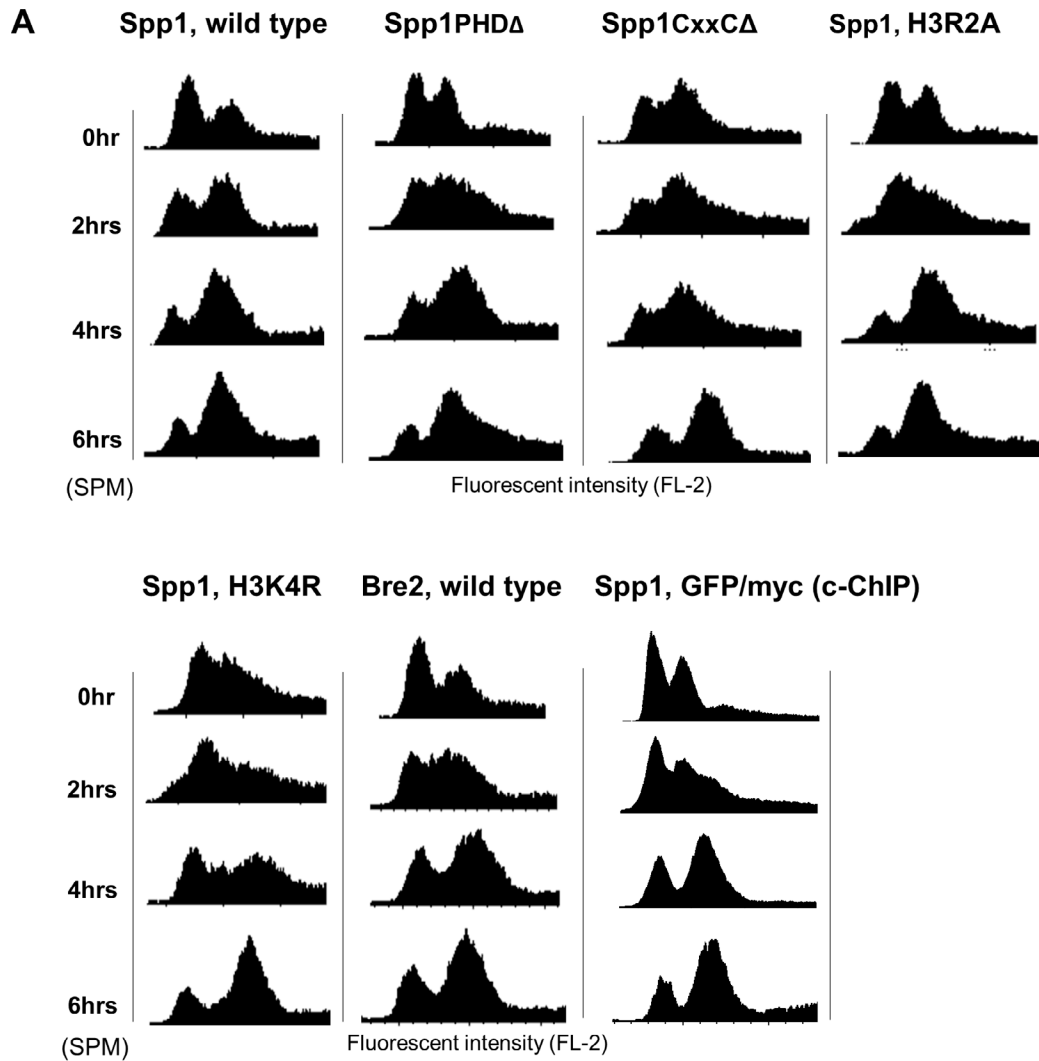
Supplemental material

Provided in a separate Excel file is Table S1, summarizing the P values related to microscopic colocalization analysis, listing the yeast strains used in this study, and providing basic NGS statistics for ChIP sequencing experiments.

Reference

Adam, C., R. Guérois, A. Citarella, L. Verardi, F. Adolphe, C. Béneut, V. Sommermeyer, C. Ramus, J. Govin, Y. Couté, and V. Borde. 2018. The PHD finger protein Spp1 has distinct functions in the Set1 and the meiotic DSB formation complexes. *PLoS Genet.* 14:e1007223. https://doi.org/10.1371/journal.pgen.1007223

A

Spp1, wild type | Spp1PHDΔ | Spp1CxxCΔ | Spp1, H3R2A

0hr, 2hrs, 4hrs, 6hrs (SPM)

Fluorescent intensity (FL-2)

Spp1, H3K4R | Bre2, wild type | Spp1, GFP/myc (c-ChIP)

0hr, 2hrs, 4hrs, 6hrs (SPM)

Fluorescent intensity (FL-2)

B

strain	spore viability (%)	sporulation efficiency (%)
Bre2-myc	95	88.7
Spp1-myc wild type	94	77.4
Spp1-myc PHDΔ	94	72.5
Spp1-myc CxxCΔ	89	69.5
Spp1-HA H3R2A	69	68.1
Spp1-HA H3K4R	70	72.4
Spp1, GFP/myc (c-ChIP)	90	73.3

Figure S1. **Meiotic progression and sporulation efficiency of yeast strains analyzed by ChIP sequencing. (A)** FACS profile of the sporulating strains measured between 0 and 6 h in SPM. **(B)** Spore viability and sporulation efficiency of the strains. The proportion of viable spores was determined by tetrad dissection (100 tetrads were dissected per strain). Sporulation efficiency was assessed by DAPI staining of nuclei (after 24 h in SPM) and counting the number of full tetrads (200 cells were analyzed in each sample).
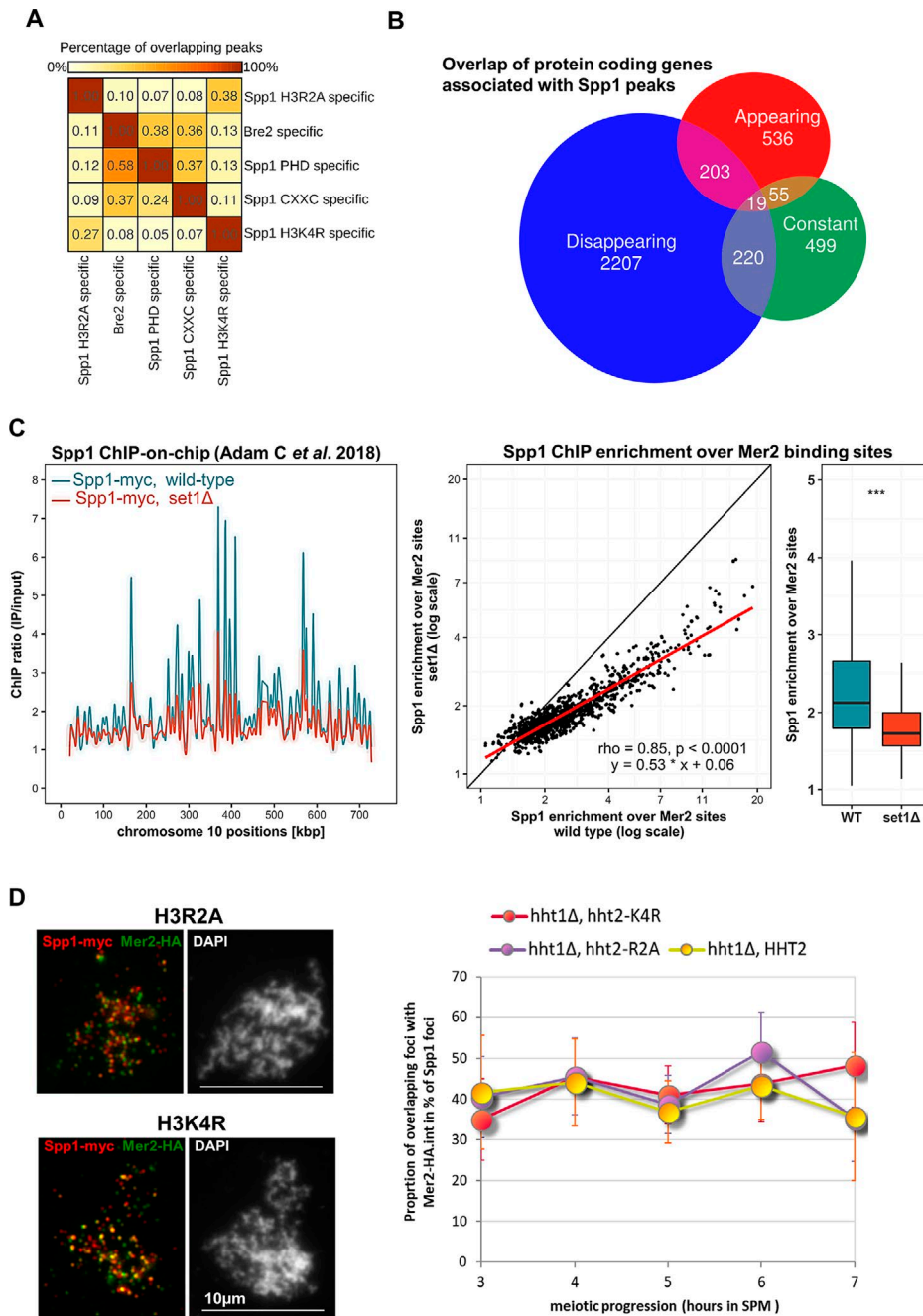
Figure S2. **Overlap analysis and ChIP enrichment of Spp1 binding sites in various mutants analyzed in this study. (A)** Heat map showing the overlap of mutant-specific Spp1 binding sites (ChIP peak positions) identified in each sample (related to Fig. 3 D). Color strength is proportional to the overlap ratio of Spp1 peak sets. The data were obtained from two biological replicate experiments. Sample sizes (n): PHDΔ-specific (183), CXXCΔ-specific (287), Bre2-specific (283), H3R2A-specific (331), and H3K4R-specific (465). **(B)** Overlap of protein coding genes associated with Spp1 peaks (related to Figs. 4, A and B; and Fig. 5 H). ORFs have been assigned to their closest Spp1 binding site and overlap ratios were visualized by proportional Venn diagrams. Number of cases (n) is indicated in the Venn diagram by the amount of differential or common ORFs associated with Spp1. **(C)** Set1-mediated histone methylation facilitates Spp1 localization on chromosomal axes (related to Fig. 3 E). Left, Spp1 ChIP-on-Chip binding profile in wild-type and *set1Δ* cells in meiosis (data are from Adam et al., 2018). ChIP enrichment profiles are shown for chromosome 10 as a representative example. Middle, meiotic Spp1 ChIP profiles over Mer2 axial sites positively correlate in wild-type and *set1Δ* cells (Spearman's rank correlation). However, the slope of regression line (red linear; 0.53) negatively deviates from the diagonal, indicating low Spp1 enrichment in the absence of Set1. Right, Spp1 enrichment at Mer2 binding sites is significantly reduced is *set1Δ* cells compared with wild-type cells. Box-whiskers plots show the medians (with interquartile ranges) of Spp1 ChIP enrichment at Mer2 binding sites. Statistically significant difference is indicated between wild-type and *set1Δ* cells (Mann-Whitney *U* test, ***, P < 0.001). The number of cases (n; Mer2 binding sites) equals to 818. **(D)** Immunofluorescent localization of Spp1-myc and Mer2-HA in the absence of modifiable H3R2 and H3K4 histone residues (related to Fig. 3 E). Left, representative chromatin spread images showing Spp1-myc foci (red) and Mer2-HA foci (green) in an H3R2A mutant (*hht1Δ* and *hht2-R2A*) and an H3K4R mutant (*hht1Δ* and *hht2-K4R*). Cells were from a meiotic time course at 4 h after transfer to SPM (SPM). DNA was stained by DAPI (white). Right, percentage of Spp1-myc foci overlapping with Mer2-HA in *HHT2, hht1Δ* (wild-type, yellow), *hht2-R2A* and *hht1Δ* (violet), and *hht2-K4R* and *hht1Δ* (red) cells. >7,000 foci were analyzed for each of the three analyzed strains. Error bars represent SD.
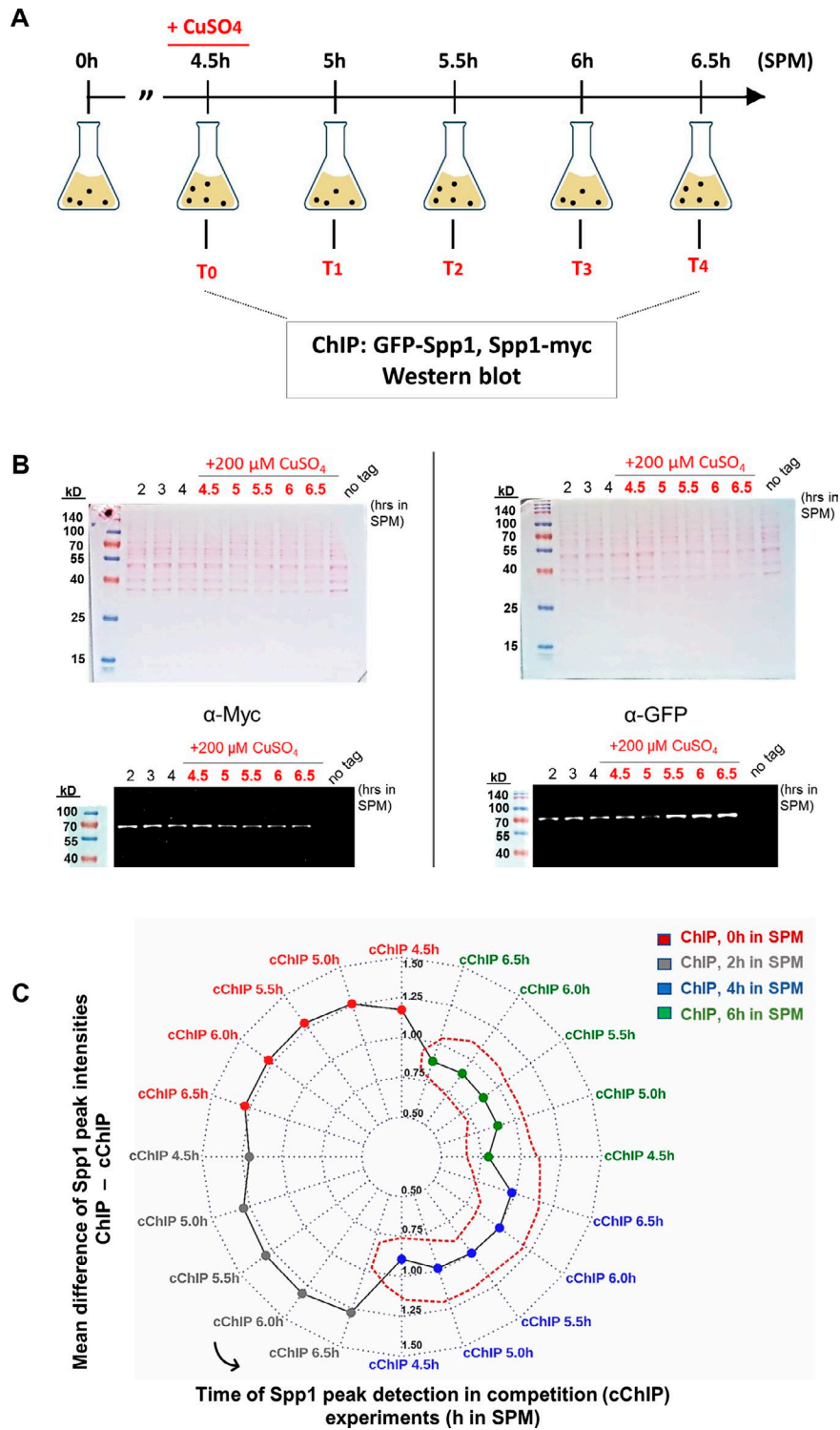
Figure S3. **Experimental design and validation of the competition ChIP experiment. (A)** Flowchart of the c-ChIP experiment. Cells were collected at various meiotic time points after addition of 200 µM CuSO₄, switching the inducible *SPP1* allele on (GFP-Spp1). Two independent biological replicate experiments were performed. **(B)** Quantitative Western blot analysis of the proper expression of constitutive Spp1-myc and inducible GFP-Spp1 proteins. Top, Ponceau staining. Bottom, detection by anti-myc and anti-GFP antibodies. The data are representative of one biological replicate experiment. **(C)** Correlation of Spp1 binding sites that were identified by c-ChIP and ChIP, represented on a polar plot. Angular positions indicate the meiotic time points, while color codes highlight the temporally compared peak sets (ChIP time points vs. c-ChIP time points). Radial grid lines define the mean differences of Spp1 IP signals (ChIP – c-ChIP). Distance from the origin is proportional to the variability of Spp1 binding sites (i.e., origin proximal datasets show high similarity between c-ChIP and ChIP). Encircled part of the polar plot (dotted red line) depicts highly ranked datasets, showing the highest similarity between 4 and 6.5 h in SPM. The c-ChIP and ChIP data are representative of two independent biological replicate experiments. Sample size (n; number of peaks): ChIP (4,524); c-ChIP (4,639).

A

	Number of Spp1 peaks	Goodness of fit parameter #
c-ChIP peaks (total)	4639	
c-ChIP peaks (fitted) *	977	**1.47 %**

* Exponential model: $\frac{GFP}{MYC} = (1 - e^{-\beta_1 * time})$

average Standard Error (SE)

B

$$y = 1 - e^{-0.047*t}$$

YFR056C (IRC7)

SE=0.0011, p-value=0.008

IRC7, chromosome 6

$$y = 1 - e^{-0.046*t}$$

YJL083W (TAX4)
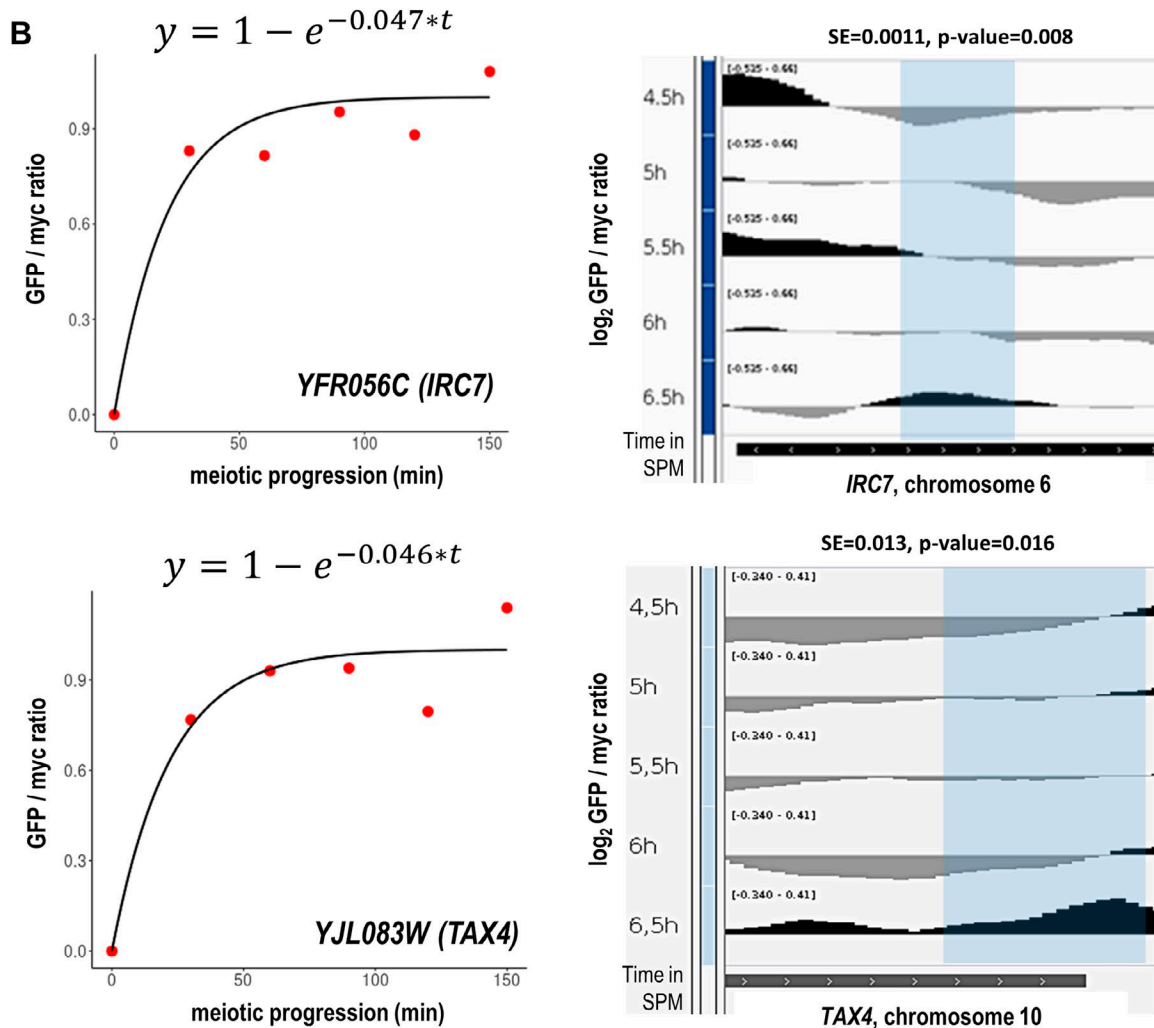
SE=0.013, p-value=0.016

TAX4, chromosome 10

Figure S4.   **Turnover rate estimation from competition ChIP data. (A)** Table showing the total number of peaks determined by c-ChIP and the number of Spp1 binding sites that could be fitted with an exponential model. The kinetic model is highlighted with an asterisk (*). Goodness of fit parameters for each binding site were estimated based on the average standard error. **(B)** Example fits of the turnover rate model for two representative Spp1 binding sites (*YFR056C* and *YJL083W*). Model equations (with standard error and P value) and temporal changes of GFP/myc ratios are shown in the left panel. JBrowse snapshots are shown on the right. The c-ChIP data are representative of two independent biological replicate experiments. Sample size (n; number of peaks): c-ChIP total (4,639); c-ChIP fitted (977).